The Sydney-AAO Multi-object Integral field spectrograph

Scott M. Croom,[1,2]* Jon S. Lawrence,[3,4] Joss Bland-Hawthorn,[1] Julia J. Bryant,[1]
Lisa Fogarty,[1] Samuel Richards,[1] Michael Goodwin,[3] Tony Farrell,[3] Stan Miziarski,[3]
Ron Heald,[3] D. Heath Jones,[5] Steve Lee,[3] Matthew Colless,[2,3] Sarah Brough,[3]
Andrew M. Hopkins,[2,3] Amanda E. Bauer,[3] Michael N. Birchall,[3] Simon Ellis,[3]
Anthony Horton,[3] Sergio Leon-Saval,[1] Geraint Lewis,[1] Á. R. López-Sánchez,[3,4]
Seong-Sik Min,[1] Christopher Trinh[1] and Holly Trowland[1]

[1]*Sydney Institute for Astronomy (SIfA), School of Physics, University of Sydney, NSW 2006, Australia*
[2]*ARC Centre of Excellence for All-sky Astrophysics (CAASTRO)*
[3]*Australian Astronomical Observatory, PO Box 296, Epping, NSW 1710, Australia*
[4]*Department of Physics and Astronomy, Macquarie University, NSW 2109, Australia*
[5]*School of Physics, Monash University, Clayton, VIC 3800, Australia*

ABSTRACT

We demonstrate a novel technology that combines the power of the multi-object spectrograph with the spatial multiplex advantage of an integral field spectrograph (IFS). The Sydney-AAO (Australian Astronomical Observatory) Multi-object IFS (SAMI) is a prototype wide-field system at the Anglo-Australian Telescope (AAT) that allows 13 imaging fibre bundles ('hexabundles') to be deployed over a 1-degree diameter field of view. Each hexabundle comprises 61 lightly fused multi-mode fibres with reduced cladding and yields a 75 per cent filling factor. Each fibre core diameter subtends 1.6 arcsec on the sky and each hexabundle has a field of view of 15 arcsec diameter. The fibres are fed to the flexible AAOmega double-beam spectrograph, which can be used at a range of spectral resolutions ($R = \lambda/\delta\lambda \approx 1700$–$13\,000$) over the optical spectrum (3700–9500 Å). We present the first spectroscopic results obtained with SAMI for a sample of galaxies at $z \approx 0.05$. We discuss the prospects of implementing hexabundles at a much higher multiplex over wider fields of view in order to carry out spatially resolved spectroscopic surveys of 10^4–10^5 galaxies.

Key words: instrumentation: spectrographs – techniques: imaging spectroscopy – surveys – galaxies: general – galaxies: kinematics and dynamics.

1 INTRODUCTION

Galaxies are intrinsically complex with multiple components and varied formation histories. This complexity is the primary reason that unravelling the physics of galaxy formation and evolution is so challenging. Galaxies are made up of baryons confined to dark matter haloes, and often have multiple distinct kinematic components (e.g. bulge and/or disc). There are complex interactions between the stars, gas, dust, dark matter and supermassive black holes. These can lead to both positive and negative feedback on the formation rate of stars.

Experimental efforts to address galaxy formation have generally taken two directions. First, galaxy imaging and spectroscopic surveys have progressively moved to higher redshift, in an attempt to directly observe galaxy evolution and formation. This approach has

had much success, placing strong constraints on the evolution of the global star formation rate (e.g. Hopkins & Beacom 2006), unveiling the strong evolution of black hole accretion over most of cosmic time (e.g. Croom et al. 2004a, 2009; Richards et al. 2006), tracing the evolution of galaxy size and morphology (e.g. Dressler et al. 1997) and much more.

The second approach has been to expand our view in wavelength rather than cosmic time. The physical processes occurring in galaxies cause emission over the entire range of the electromagnetic spectrum. In order to have a full picture of galaxy formation, a multi-wavelength approach is vital. This has been made more achievable with recent generations of satellites covering the X-ray, ultraviolet, mid- and far-infrared. While the spectral energy distributions (SEDs) of stars tend to peak in the optical or near-infrared, obscuration and reprocessing by dust generate strong mid- and far-infrared emission. Young stars (when not obscured) are most directly traced in the ultraviolet, while black hole accretion can generate radiation

*E-mail: scroom@physics.usyd.edu.au

from the radio to X-ray and gamma-ray bands. Surveys such as the Galaxy And Mass Assembly (GAMA) survey (Driver et al. 2011) and the Cosmic Evolution Survey (COSMOS; Scoville et al. 2007) show the value of this multi-wavelength approach.

The third route, and the one that we address in this paper, is to focus on spatially resolving galaxies, in particular, obtaining spatially resolved spectroscopy. Optical spectroscopy allows us to measure a wide range of parameters including current star formation rates (e.g. via Hα), gas phase metallicities, stellar ages, stellar metallicities, black hole accretion rates, ionization structure and extinction due to dust (e.g. via the Balmer decrement). The major spectroscopic surveys to date have used a single fibre (Colless et al. 2001; Abazajian et al. 2003) or single slit (Le Fèvre et al. 2005; Davis et al. 2007) on each object, and so obtain just one measurement of these parameters for each galaxy. Moreover, these measurements may not be representative of the galaxy as a whole, but biased, depending on where the aperture is placed. This fundamental problem is addressed by integral field spectrographs (IFS). In the last decade, projects such as SAURON (Bacon et al. 2001) have demonstrated the power of integral field spectroscopy to capture a range of key observables that are simply not available to single-aperture surveys. As well as studying the properties listed above in a spatially resolved context, obtaining gas and stellar kinematics over an entire galaxy enables us to separate dynamical components, measure dynamical mass, examine the impact of winds and outflows, and discover merging systems via dynamical disturbances.

Integral field spectroscopy has almost exclusively been limited to single-object instruments, meaning that it is time-consuming to build large samples. The largest current data set, using the SAURON system on the William Herschel Telescope, contains ∼260 objects (ATLAS-3D; Cappellari et al. 2011a). The Calar Alto Legacy Integral Field Area Survey (CALIFA) project (Sánchez et al. 2011) aims to target 600 objects with the Potsdam Multi Aperture Spectrophotometer (PMAS) integral field unit (IFU) on the Calar Alto Telescope using ∼200 nights of telescope time. The only multi-object IFS currently available is that on the VLT Fibre Large Area Multi Element Spectrograph (FLAMES) instrument (Pasquini et al. 2002), which contains 15 IFUs, each with 20 spatial elements of size 0.52 arcsec and a total field of view (FoV) of 2×3 arcsec. This has enabled measurements of the Tully–Fisher relation (TFR) at ∼0.6 (Yang et al. 2008) as well as a number of other projects. However, the small FoV of each IFU, combined with the high spectral resolution (≥9000) and associated narrow wavelength range, limits its applicability for large-scale surveys.

Astrophotonic technology (Bland-Hawthorn & Kern 2009) is now opening the way to new instrumentation that can address the need for highly multiplexed integral field spectroscopy. Hexabundles (Bland-Hawthorn et al. 2011; Bryant et al. 2011) are optical fibre bundles where the cladding has been stripped from each fibre to a minimum over a short length (∼30 mm) and the fibres then gently fused together at the input end to provide an IFU (∼1 mm aperture) with high filling factor. These can then be used in conventional multi-fibre spectrographs.

In this paper, we report on the Sydney-AAO (Australian Astronomical Observatory) Multi-object Integral field spectrograph (SAMI), the first fully operational demonstrator instrument to use hexabundles. SAMI has 13 IFUs that can be positioned anywhere over a 1-degree diameter FoV. In Section 2, we discuss in detail the scientific rationale for such an instrument, along with some practical considerations regarding sensitivity. In Section 3, we describe the SAMI instrument in detail. In Section 4, we outline the observations

carried out during the commissioning of the instrument, the results from which are discussed in Section 5. Our conclusions, and goals for the future, are laid out in Section 6.

2 SCIENTIFIC RATIONALE

In this section we outline the key scientific drivers for an instrument such as SAMI. The fundamental question at the heart of this work is: how did the galaxy population we see around us today come about? This requires us to understand the physical processes that occur as galaxies form and evolve. The galaxy population we see today has some very distinctive features that need to be explained.

One of the most fundamental points is the separation of galaxies into a bimodal distribution according to colour (e.g. Strateva et al. 2001; Baldry et al. 2004). A galaxy's colour is primarily related to the presence of ongoing star formation. The second key feature differentiating galaxies is morphology. There is a strong correlation between colour and morphology, with galaxies lying along the 'red sequence' being mostly passive systems with elliptical/spheroidal morphology, while galaxies inhabiting the 'blue cloud' are mostly dominated by discs, although this is not always strictly the case (e.g. Schawinski et al. 2009; Masters et al. 2010). While they are related, there is not a strict one-to-one relationship between morphology and colour. A clearer understanding of galaxies can be obtained if they are considered as being made up of distinct morphological components (discs, bulges and pseudo-bulges) that result from different formation processes and evolutionary histories (Driver et al. 2007). The intrinsic properties of these structural components are more uniform than those of the galaxies they compose. Their formation pathways are also quite different, with true bulges built up by violent mergers, discs from gas accretion and pseudo-bulges from secular evolution (Kormendy & Kennicutt 2004). Disentangling these various modes is complex, but can be materially aided by the fact that the structures formed have different kinematic properties as well as different star formation histories.

In order to ascertain the physics involved, we need to determine the answers to a number of questions that broadly fall into four categories: (i) how does galaxy mass and angular momentum build up? (ii) when, where and why does star formation occur? (iii) when, where and why does black hole accretion occur? (iv) how are galaxies fuelled and what is the role of feedback? We will discuss each of these issues in turn, although there is of course significant overlap between them.

2.1 The build up of mass and angular momentum

The standard picture of galaxy formation has gas cooling to form a rotationally supported disc within a cold dark matter halo (White & Rees 1978). While this picture is broadly accepted, feedback and interactions provide major complications which are not yet fully understood.

The scaling relation between circular velocity and stellar mass (TFR; Tully & Fisher 1977) for disc galaxies provides a tight constraint for galaxy formation models. The circular velocity depends on the ratio of disc mass to halo mass, the dark matter halo profile and the dimensionless spin parameter, λ (Peebles 1969). The largest TFR samples (e.g. Springob et al. 2007) currently contain ≃5000 galaxies with either long-slit spectroscopy or spatially unresolved H I velocities. If IFU observations can be made out to large enough radii (typically ∼2.2 disc scale lengths), then they provide substantial advantages in allowing a clearer picture of distorted kinematics and inclination. Circular velocities can be compared to the results

of galaxy lensing to constrain the dark matter halo profile and examine evidence of contraction of the halo in response to the baryons (Dutton et al. 2010; Reyes et al. 2011).

The stellar and emission line kinematic data that SAMI can provide will allow dynamical mass estimates within maximum radius probed, using techniques such as anisotropic Jeans modelling (Cappellari 2008). In general, it is not possible to determine total mass because of the uncertainty of the dark matter halo parameters. Even for the Milky Way, where many halo stars can be used to probe the outer halo, the total galaxy mass is uncertain to a factor of 2 (Smith et al. 2007). Detailed dynamical techniques are in stark contrast to estimates of dynamical mass which simply take a single velocity dispersion of the galaxy (e.g. from a single fibre observation; e.g. Taylor et al. 2010).

It is relatively easy to extract a rotation curve $v(r)$ from the observed data if the kinematics are fairly well ordered (Staveley-Smith et al. 1990). This can then be used to provide dynamical information about the galaxy, particularly if baryonic information is brought to bear. However if the kinematic axes are misaligned with the photometric axes, this is often a signature of streaming motions due to a bar or an oval distortion. A dynamical mass can still be derived, although the increased number of free parameters makes this more uncertain (Staveley-Smith et al. 1990; Quillen, Frogel & Gonzalez 1994). Any deviations from rotational symmetry are important in their own right. It is often very difficult to see the presence of bars, particularly in highly inclined disc systems. But bars are often betrayed by the inner twists of the isovelocity contours. Warps are more easily detected on large scales and almost always in H I kinematics (Briggs 1990); however, the same effects can now be seen in deep observations of the diffuse ionized gas in the outer disc (Christlein, Zaritsky & Bland-Hawthorn 2010). The physical cause of kinematic distortions can be examined by large IFU surveys which probe a variety of galaxy parameters. For example, are distortions more likely in high-density regions due to dynamical interaction.

Integral field spectroscopy also enables studies of stellar kinematics that describe the observed projected stellar angular momentum per unit mass of galaxies, not possible with other techniques (Emsellem et al. 2007, 2011; Brough et al. 2011). This measurement enables the separation of early-type galaxies into fast and slow rotators which are thought to have very different formation paths. A great success of the SAURON and ATLAS-3D projects (Bacon et al. 2001; Cappellari et al. 2011a) has been the discovery that most early-type galaxies have significant rotation, with only $\simeq 14$ per cent (predominantly at high mass) being slow rotators. Cappellari et al. (2011b) have used ATLAS-3D to demonstrate a kinematic morphology–density relation, which shows a smooth transition of spirals to early-type fast rotators with increased density, and massive slow rotators only inhabiting the highest density regions. SAMI would allow such studies to be expanded to probe greater dynamic range in environment and examine such relations as a function of stellar mass.

The rate of dark matter halo merging can be accurately estimated from simulations (Fakhouri & Ma 2008). Kinematic information from integral field spectroscopy can be used to differentiate between quiescent galaxies and those undergoing a merger (e.g. Shapiro et al. 2008), using procedures such as kinemetry (Krajnović et al. 2006). Until now, this type of analysis has largely been limited to high redshift (where the merger rate is expected to be higher), but with samples of 10^3 or more galaxies, statistically meaningful estimates of merger rates can be made at low redshift. Fakhouri & Ma (2008) predict that the halo merger rate at $z \sim 0$ should be ~ 0.05 halo^{-1} Gyr^{-1}

for major mergers (with mass ratios $< 3/1$). Integral field observations provide a complementary approach to studies which focus on the number of close pairs to estimate merger rates (e.g. De Propris et al. 2007), as they probe very different phases of the merger process. It is also be possible to look for weaker dynamical disturbances in discs due to repeated minor mergers/interactions (Zaritsky & Rix 1997). In this case, it is very advantageous to extend the study to large radius as the effect of tidal perturbations scales as $\sim r^3$. In this case the challenge is to achieve sufficient sensitivity at large radius (e.g. $\gtrsim 1.5$–2 scale lengths).

Spin angular momentum from galaxy kinematics can directly probe the formation of the large-scale structure of the Universe and galaxy formation. The spin of galaxy discs provides an approximation of the spin of the galaxy's dark matter halo (Sharma & Steinmetz 2005), which is coupled to the large-scale structure. Early in a dark matter halo's life, it experiences torques from the surrounding density landscape. The spins of dark matter haloes today retain some memory of that landscape, so spin is intrinsically linked with the large-scale structure. This link may be examined in N-body simulations and observations by measuring the distribution of inferred dark matter halo spin magnitude (Berta et al. 2008) and by the relative orientation of galaxy spin directions with each other and with the large-scale structure.

N-body simulations do not predict a strong alignment between the spins of neighbouring haloes, although an alignment between galaxies has been detected in the Tully catalogue of 12 122 nearby spirals (Pen, Lee & Seljak 2000). Simulations and theory predict an alignment between halo spin and the tidal field (Lee & Pen 2000), and an alignment with features in the tidal field like filaments (Zhang et al. 2009), sheets (Lee 2004) and voids (Brunino et al. 2007). Any kind of alignment is predicted to be very weak, however, so could only be seen in large-scale galaxy surveys. There have been detections of spin alignments in the large-scale structure reconstructed from imaging surveys (Lee & Erdogdu 2007; Paz, Stasyszyn & Padilla 2008), using inferred galaxy spins from disc shapes. A tentative detection of spin alignment with filaments was found using the inferred spin of only 201 galaxies around voids (Trujillo, Carretero & Patiri 2006) and 70 galaxies in filaments (Jones, van de Weygaert & Aragón-Calvo 2010), picked from the large-scale structure of Sloan Digital Sky Survey (SDSS). Discrepancies between the results found from dark matter simulations and observations indicate a difference in the way that galaxies and dark matter haloes obtain and keep their spin. A large survey of direct spin measurements could reveal whether galaxies exhibit the same spin behaviour as dark matter haloes, and show how galaxy spin is linked to the large-scale structure.

2.2 When, where and why does star formation occur?

Much recent observational and theoretical work has focused on how blue galaxies can have their star formation quenched, moving them on to the red sequence. Red sequence galaxies are preferentially found in denser environments (e.g. Blanton et al. 2005), and star formation is also clearly suppressed at high density (e.g. Lewis et al. 2002). This immediately suggests environmental factors play an important role. When a galaxy falls into a cluster, the ram pressure from the dense intergalactic medium (Gunn & Gott 1972) may expel the gas from the disc, removing the fuel required for further star formation. There are several observed examples of this in rich clusters (e.g. Sun, Donahue & Voit 2007; Randall et al. 2008). In moderately dense regions, such as galaxy groups, it may be that ram pressure will leave the disc intact, but can still remove gas from the

halo of the galaxy. The halo provides a reservoir of gas which can replenish the disc.

Without the halo gas, the star formation will decline and then cease as the disc gas is consumed, leading to a transition to the red sequence, in a process known as strangulation (Larson, Tinsley & Caldwell 1980). Simulations suggest that this process can be efficient at removing halo gas, even in small and/or compact groups (Bekki 2009; McCarthy et al. 2008), but there is little direct experimental evidence that this is the case. Indirect evidence does point to some pre-processing of galaxies in groups before they fall into clusters (Balogh & McGee 2010), but the physical process driving this is not clear. Direct galaxy–galaxy interactions are also expected to play a critical role, with major galaxy mergers triggering star formation (e.g. Ellison et al. 2008) and transforming the morphology of galaxies, although the fraction of galaxies undergoing major mergers (i.e. those with mass ratios of 3:1 or less) in the local Universe is small (e.g. Patton & Atfield 2008). On the other hand, dwarf star-forming galaxies in the local Universe are often found interacting with low-luminosity objects or diffuse H I clouds. This appears to be the triggering mechanism of their intense star formation activity (López-Sánchez & Esteban 2008, 2009), although only detailed multi-wavelength observations are able to reveal these processes (López-Sánchez 2010; Lopez-Sanchez et al. 2011).

However, environment is only one factor. Feedback from star formation and accretion on to supermassive black holes provide an internal mechanism for transformation. This feedback provides a solution to the mismatch of the theoretical dark matter halo mass function and the observed stellar mass function (e.g. Baldry, Glazebrook & Driver 2008) by heating and/or expelling gas in both low-mass (via star formation) and high-mass (via black hole accretion) haloes (Cattaneo et al. 2006; Baldry et al. 2008). Extreme outbursts of star formation or black hole accretion may be triggered by mergers or interactions (e.g. Hopkins et al. 2008), making a link between internal and environmental effects. Once the burst is over, another mechanism is needed to suppress continued star formation. The best suggestion for this is mechanical feedback from jets emitted by supermassive black holes (e.g. Croton et al. 2006), but this only appears to be efficient in massive galaxies.

As well as these active processes, the environment has an indirect influence via formation age. Galaxies in high-density regions form earlier and so have had more time to evolve (e.g. Kaiser 1984; Bardeen et al. 1986; Thomas et al. 2005). In the absence of other effects, we would then expect to see galaxies in high-density regions having older stellar populations.

Disentangling these varied influences on galaxy formation is far from trivial. However, studies of the spatial distribution of instantaneous star formation rates, integrated star formation (via stellar population ages) and metallicity (both gas and stellar) provide considerable insight. Importantly, ram-pressure removal of gas implies that the truncation of star formation is an *outside-in* process (e.g. Bekki 2009; Kapferer et al. 2009). Gas is preferentially removed in the outer parts of galaxies, which are less gravitationally bound. This may be a short-lived feature of the galaxies in dense environments if the gas is eventually completely removed. Alternatively, stripping can occur over the lifetime of a galaxy if the gas is puffed up by the internal star formation; in this case, even a rarified external medium can remove gas from the galaxy (Nichols & Bland-Hawthorn 2011). Globally, the expectation would be that galaxies form inside-out, and this implies age and metallicity gradients which are observed (e.g. Shaver et al. 1983; Vila-Costas & Edmunds 1992; Steinmetz & Mueller 1994; Chiappini, Matteucci & Gratton 1997).

One approach that has been explored in some detail as an alternative to spatially resolved spectroscopy is the so-called 'pixel-*z*' technique (Conti et al. 2003; Welikala et al. 2009, 2008). This approach, analogous to photometric redshifts ('photo-*z*'), uses a library of template SEDs to fit the observed optical and near-infrared colours of individual pixels within resolved galaxy images. This technique has been used with some success to explore the environmental dependence of star formation in galaxies. Welikala et al. (2008) find that, globally, the suppression of star formation in high-density environments (e.g., Lewis et al. 2002; Gómez et al. 2003) seems to occur primarily in the most strongly star-forming population, and to be evidenced by a suppression in the *inner* regions of galaxies. Welikala et al. (2009) demonstrate that this effect seems to hold independently for both early- and late-type galaxy populations, and that the suppression in star formation cannot be explained solely by the well-known density–morphology relation (e.g., Dressler 1980). There are significant limitations, however, to the 'pixel-*z*' approach. These are related to implicit assumptions made by the technique, such as each pixel being represented by an isolated single stellar population with a simple exponential star formation history (Conti et al. 2003; Welikala et al. 2008). As a result, the method cannot effectively measure the instantaneous star formation rate, which can be traced spectroscopically (e.g. by Hα emission).

IFU spectroscopy allows us access to both current star formation (via emission lines) and integrated star formation history (via stellar age and metallicity). Examining the radial dependence of the mean stellar age and metallicity gradients tells us when and where the stars formed in these galaxies, along with a fossil record of the galaxy merger history. The mean stellar age is effectively a luminosity-weighted integral of the star formation history whilst the stellar metallicity gradient provides an indication of its merging history (e.g. Kobayashi 2004). If environmental effects are responsible for the cessation of star formation, then we would expect red sequence galaxies to have younger central ages with past major mergers sign-posted by shallow negative metallicity gradients (i.e. lower metallicities in the outskirts; Kobayashi 2004; Brough et al. 2007; Spolaor et al. 2009).

2.3 When, where and why does black hole accretion occur?

A full picture of the physical processes involved in the fuelling of accretion on to supermassive black holes, resulting in the phenomenon of an active galactic nucleus (AGN), is still elusive. It is now known that most galaxies contain supermassive black holes, with typical masses a million to a billion times that of the Sun (e.g. Gebhardt et al. 2000; Ferrarese & Merritt 2000). The mass of the black hole correlates well with the mass (or velocity dispersion) of the bulge or spheroidal component (Tremaine et al. 2002) in a galaxy. This implies an intimate connection between the build up of stellar mass in galaxies and their supermassive black holes.

The nature of the connection between star formation and AGN has long been debated (e.g. Sanders et al. 1988), although a resolution remains elusive. The most luminous AGN (i.e. bright quasars) require $\gtrsim 10^9$ solar masses of gas deposited in their central regions on time-scales of $\sim 10^7$–10^8 yr (e.g. Croom et al. 2005), requiring major galaxy-wide perturbations (Hopkins & Hernquist 2009), and no doubt triggering substantial star formation. In contrast, low-luminosity AGN require relatively small amounts of gas, which can be supplied by internal stochastic processes, such as the accretion of cold molecular clouds (Hopkins & Hernquist 2009).

The AGN population evolves strongly with cosmic time. This is most clearly seen in evolution of luminous quasars from $z = 0$ to $z \simeq 6$ (Richards et al. 2006; Croom et al. 2009), which have a strong peak in space density at $z \simeq 2$–3. Lower luminosity AGN show less severe evolution, and peak in space density at lower redshift (e.g. Hasinger, Miyaji & Schmidt 2005; Croom et al. 2009). This downsizing appears qualitatively similar to that seen in the formation of galaxies (Cowie et al. 1996). In the local Universe, accretion on to black holes is dominated by systems with low black hole masses, $<10^8 \, \mathrm{M}_\odot$, but which are typically accreting within an order of magnitude of the Eddington limit (Heckman et al. 2004). In contrast, higher mass black holes in the local Universe are accreting with a characteristic time-scale substantially longer than a Hubble time.

Luminous AGN (as measured by their [O III] $\lambda 5007$ luminosity) are found to have younger stellar populations (Kauffmann et al. 2003), as measured by their $D_n(4000)$ and Hδ line indices from SDSS spectra. It is not clear whether this younger stellar population is centrally concentrated, or is distributed more widely across the host galaxy, as the SDSS fibres subtend a physical scale of $\sim$5 kpc at $z = 0.1$. IFS data have the ability to explicitly examine the distribution of star formation and stellar population ages across galaxies and investigate whether these are related to accretion rate.

Lower luminosity AGN tend to have spectra typical of Low-Ionization Nuclear Emission-line Regions (LINERs; Heckman 1980). While there is evidence that these form a continuous sequence with Seyferts (Kewley et al. 2006), there is substantial evidence that LINER-like emission is extended and may be powered by ionization from asymptotic giant branch stars (Yan & Blanton 2011). A large galaxy survey with spatially resolved spectroscopy could resolve this issue. If LINER emission is not due to a central AGN in most cases this would require substantial re-interpretation of recent work on low-redshift AGN. At an even more fundamental level, the fraction of galaxies which host AGN is only well defined locally (i.e. tens of Mpc; Ho 2008). Approximately 40 per cent of these very local galaxies host AGN. At larger distances contamination from off nuclear emission increasingly reduces the sensitivity to weak nuclear emission lines. A large IFS survey would enable apertures of fixed metric size to be defined, enabling robust AGN rates as a function of redshift to be determined.

While there is a good theoretical basis for galaxy mergers triggering luminous AGN (e.g. Hopkins & Hernquist 2009), the evidence for this is mixed. An alternative pathway is via violent disc instability in self gravitating discs (e.g. Bower et al. 2006; Bournaud et al. 2011). Disc instability is at least likely to play a role at high redshift where cold streams can dominate the mass accretion on to discs (Dekel et al. 2009). Indeed, a large fraction of high-redshift star-forming galaxies appear to be discs (e.g. Genzel et al. 2008; Wisnioski et al. 2011), rather than mergers. In low-redshift samples AGN activity is not enhanced by the presence of a nearby companion (Li et al. 2008b), while star formation is (Li et al. 2008a). This is a somewhat surprising result, and may point to a difference in time-scale between the onset of star formation and the AGN, with the AGN occurring later, after the merger has taken place. Indeed, IFS observations of local galaxies with observed outflows demonstrate that the AGN time-scale is significantly longer than the starburst time-scale (Sharp & Bland-Hawthorn 2010). Large-scale IFS observations can directly address the issue of AGN fuelling by examining the kinematic properties of AGN hosts, and searching for evidence of disc instability and/or merging. In this regard it will be particularly important to span a range of accretion luminosities in order to examine whether there is a change from secular evolution at low accretion rate to mergers at high accretion rate.

2.4 Feeding and feedback

The accretion of gas on to galaxies remains a largely unsolved problem. Whether gas enters the galaxy potential in a hot phase and then cools down (Binney, Nipoti & Fraternali 2009), as a warm rain (Bland-Hawthorn et al. 2007), or as an H I complex like the high-velocity clouds in the Galactic halo (Sancisi et al. 2008), or all of the above, is unclear. After a review of the evidence, Binney (1992) concluded that the outer warps of H I discs were some of the best evidence of ongoing disc accretion. Once the gas settles into the galaxy, the outstanding issues are how the gas feeds into the nuclear regions and, in particular, on to a central black hole.

In a survey of 10^3–10^4 galaxies, SAMI offers the prospect of studying nuclear activity (AGN, starburst, LINER) and star formation within the context of the extended galaxy. The kinematic signatures of outer warps and inner bar streaming are relatively easy to pick out in H I (Staveley-Smith et al. 1990) or in ionized gas (Christlein et al. 2010). Thus, we can now directly associate this activity with large-scale disc disturbances, assuming these exist. Traditionally, in large galaxy surveys, the association of activity and dynamical disturbances is made from the proximity of galaxies in position and redshift space (e.g. Nikolic, Cullen & Alexander 2004; Li et al. 2008a). With full kinematic information a much more direct determination of the triggering of activity will be possible.

An alternative approach is to study the impact of the inner disc on the extended properties of galaxies (e.g. Martin 1998; King & Pounds 2003). Jets carry energy, and winds carry gas and metals, far from the nucleus. In a recent integral field study of 10 AGN and starburst galaxies, Sharp & Bland-Hawthorn (2010) find that starburst winds are largely shock ionized, while AGN winds show the hallmark of photoionization by the accretion disc, clearly indicating that the starburst phenomenon is very short. For one of the objects observed on the SAMI commissioning run, we see the ionization characteristics typical of nuclear activity for gas off the plane of an inclined disc (see Section 5.4 and Fogarty et al., in preparation). A large-scale wind is confirmed by the broad emission-line profiles along the minor axis. This is a remarkable testament to the power of spatially resolved kinematic and ionization information. In the full survey, SAMI is likely to uncover hundreds of new outflow sources connected to either nuclear activity or inner disc star formation. There is an even rarer class of galaxies with disc-wide winds that SAMI will also inevitably add to (Strickland 2007).

A number of edge-on spiral disc galaxies have vertically extended ionized gas in their haloes (Rand 1996; Dettmar 1992). The Reynolds Layer in our Galaxy, recently mapped by the Wisconsin Hα Mapper (Madsen, Haffner & Reynolds 2006), is a good example of this phenomenon (see also Gaensler et al. 2008). The ionization characteristics of this gas do not appear to be consistent with any known mechanism (i.e. UV photoionization by hot young stars, radiation from old supernova bubbles, shocks from supernovae, cosmic ray heating, or radiation pressure on dust grains in the disc). The gas may arise from some kind of disc-wide interaction between the disc and the hot halo, presumably driven by processes related to star formation in the disc (Cox 2005). But there is also the prospect that some of this gas is related to warm gas accretion on to the disc (Bland-Hawthorn 2009) or involved in a large-scale circulation or recycling of gas through the halo (Marinacci et al. 2011).

As with the study of galaxy winds, a large SAMI survey has the potential to greatly increase the sample of known galaxies with

vertically extended warm discs. With a larger sample, it will be possible to correlate the presence of these discs with the disc star formation rate, nuclear activity and galaxy mass.

2.5 Limitations of current spectroscopic surveys

Historically, telescopes were used to observe one source at a time. But with technical advances in optical fibres, it was realized in the early 1980s that many sources could be observed simultaneously across the telescope focal plane by precisely positioning fibres in the field (Barden, Ramsey & Truax 1981; Gray 1983). This led to an explosion in wide-field spectroscopic surveys, notably including the 2-degree Field Galaxy Redshift Survey (2dFGRS; Colless et al. 2001), 2-degree Field QSO Survey (2QZ; Croom et al. 2004a), 6-degree Field Galaxy Survey (6dFGS; Jones et al. 2009) and SDSS (York et al. 2000) amongst several others. Between them, such surveys have obtained spectra for approximately 1.5 million extragalactic targets. New instruments recently commissioned [e.g. the Large Sky Area Multi-object Fibre Spectroscopic Telescope (LAMOST); Su et al. 1998] or in construction (e.g. the Visible Integral-field Replicable Unit Spectrograph (VIRUS); Hill et al. 2004) are able to observe thousands of sources at a time.

Considerable advances have been made possible by the 2dFGRS and SDSS, which use a single optical fibre per galaxy. However, with fibre diameters of 2 and 3 arcsec, respectively, these projects sample less than half the light from a galaxy at the median distance of the surveys. These single apertures limit the surveys in two ways.

First, it is impossible for single-fibre surveys to measure spatially varying spectral properties, which prohibits the study of crucial observables such as kinematic merger rates, galaxy rotation and dynamical mass, star formation gradients, metallicity gradients, age gradients and detection of galaxy winds and/or outflows.

The second limitation is that with single-fibre spectroscopy the measured signal depends on many things: (i) intrinsic properties, like source luminosity, size and distance; (ii) atmospheric conditions, particularly seeing; (iii) instrumental properties, like fibre aperture size and positioning accuracy, and optical focus over the field; (iv) telescope properties, such as pointing and guiding precision; and perhaps other effects. Many published papers make the mistake of assuming the surveys provide *spectrobolometry* (i.e. the spectrum of the total light output by the source) rather than the spectrum from a (often ill-defined) spatial sample of the source. The inherent dangers of aperture effects have long been known in astronomy, but have often been underappreciated or ignored. Ellis et al. (2005, see their fig. 8) clearly demonstrate that the single-aperture fibre spectra from a typical galaxy survey may be only weakly correlated with the photometric classification.

Aperture biases can manifest themselves in two ways. The fibres subtend an increasing linear size with increasing distance of the galaxy, potentially causing spurious evolutionary effects (and spurious luminosity-dependent effects in a flux-limited sample). Secondly, important galaxy properties, such as star formation rate and metallicity, can have substantial gradients, meaning that observations of just the central regions are not representative of global values (e.g. Kewley & Ellison 2008).

2.6 Why multiplexed IFUs?

Integral field spectroscopy allows us to gather data on key observables that are simply inaccessible to single apertures. IFUs are usually a single monolithic array of lenslets, with the light fed to

a spectrograph via optical fibres (or alternatively an optical image slicer). As a consequence, they can only target one object at a time and so IFU surveys have typically only targeted a few tens of galaxies in specific classes (e.g. Emsellem et al. 2007; Pracy et al. 2009).

The process of galaxy formation and evolution is inherently complex, with the observed galaxy properties depending on a large number of parameters, such as host halo mass, stellar mass, merger history, etc. As well as the multi-dimensional nature of galaxy properties, there is inherent stochasticity in the process. This is at least in part due to our inability to accurately trace the formation history of individual objects, but also derives from inherently non-linear physics such as that involved in the collapse of molecular clouds to form stars.

The multi-dimensional nature of the galaxy population, combined with this stochasticity (which at some level could be considered as extra hidden parameters), means that large surveys are required to extract the key relations between physical properties. The success of surveys such as 2dFGRS and SDSS has in large part been due to their ability to 'slice and dice' the galaxy distribution and still have statistically meaningful samples in each bin of the parameter space.

The need to extend integral field observations to large samples is well understood in the above context, and has driven recent projects such as ATLAS-3D (Cappellari et al. 2011a) and CALIFA (Sánchez et al. 2011). These impressive projects are limited by their use of monolithic IFUs, which means that targeting more than a few hundred objects is prohibitively expensive in terms of telescope time. This limitation naturally drives us to multi-object integral field spectroscopy (i.e. multiplexed IFUs), the subject of this paper.

2.7 Size and surface brightness

A key challenge for multi-object integral field spectroscopy is to obtain sufficient signal-to-noise ratio (S/N) at low surface brightness levels for all the targets observed simultaneously in a given pointing. In this section we present some preliminary investigations of the properties of potential SAMI targets. We will use the recent Sérsic fits and bulge–disc decomposition carried out by Simard et al. (2011) on the SDSS photometry.

First we consider a simple apparent-magnitude-limited sample with $r_{ser} < 16.5$ (extinction corrected, where r_{ser} is the galaxy SDSS r-band magnitude derived from a Sérsic model fit to the photometry). This limit was chosen as the galaxy surface density approximately matches the density of IFUs in SAMI. The distribution of half-light radius, R_e, and surface brightness at R_e is shown in Fig. 1. For such a sample the SAMI hexabundle IFUs reach to $1R_e$ for all but the largest 10 per cent of galaxies (blue dashed line), while $1R_e$ is sampled by at least three IFU elements for all but the smallest 10 per cent of galaxies. In other words, for the central 80 per cent of this sample, SAMI can give spatially resolved spectroscopy out to at least $1R_e$. The median surface brightness at $1R_e$ is $\mu_e \simeq 22$ mag arcsec^2.

We show how size and surface brightness vary with redshift for this sample in Figs 2(a) and (b). The typical sizes in arcsec of the galaxies stay relatively constant with redshift, largely because the r-band limit selects more massive (and therefore larger) galaxies at higher redshifts. A natural alternative is to select a volume-limited sample, which is shown in Figs 2(c) and (d). In this case we choose $M_r < -19.5$ and $z < 0.075$, which gives similar numbers of targets (i.e. similar surface density) to the r-band cut used above. In this case we see, unsurprisingly, that the galaxies are smaller at high
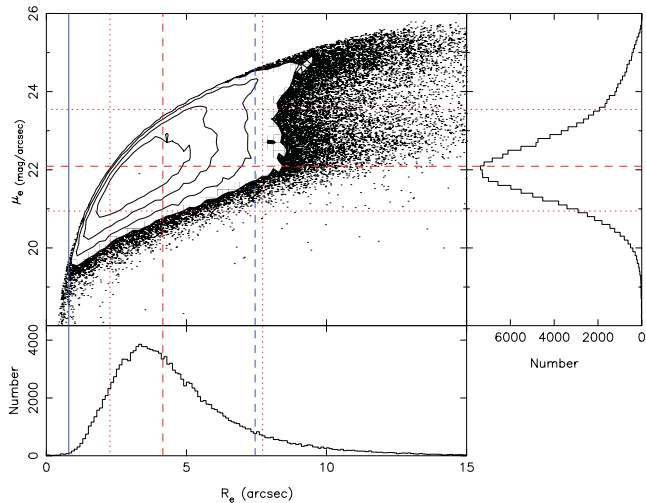
Figure 1. The size–surface brightness distribution for an *r*-band sample of SDSS galaxies limited to $r_{ser} < 16.5$ (extinction corrected). Size is defined as the half-light radius, R_e, and the surface brightness, μ_e, is also given at this radius. The marginal distributions of size and surface brightness are shown below and to the right of the main panel. Red dashed lines show the median of each parameter, while the dotted red lines show the 10th and 90th percentiles of the distributions. The blue solid line marks the radius of a single fibre core in SAMI and the blue dashed line is the radius of the 61-core hexabundle.

Figure 2. Size and surface brightness as functions of redshift for a magnitude-limited galaxy sample with $r_{ser} < 16.5$ (panels a and b) and for a volume-limited sample with $M_r < -19.5$ and $z < 0.075$ (panels c and d). The black solid line is the median and the black dotted lines are the 10th and 90th percentiles. The blue solid line is the radius of a single fibre core in SAMI and the blue dashed line is the radius of a 61-core hexabundle.

redshift, but that the median R_e is more than twice the radius of a fibre core (and more than three fibre cores out to $z \simeq 0.06$).

An apparent-magnitude-limited sample can be considered as a set of volume-limited samples with small redshift intervals and absolute magnitude limits that vary with redshift. It is highly likely that the optimal solution for targeting galaxies for a multi-object IFU instrument involves taking multiple volume-limited samples, allowing optimal use of the IFU FoV while broadly populating the distribution of galaxy stellar mass. One issue that needs to be considered is that in an apparent-magnitude-limited sample, objects inevitably pile up around L^*, so suitable sampling may need to be implemented to efficiently cover a wide range in stellar mass.

Last considerations in target selection include whether to sample all the galaxies in a given volume or to choose field locations which uniformly sample the distribution of galaxy environment. The challenge with the latter approach is that there are a variety of different local density estimators and the relation between them is not trivial (see Brough et al., in preparation). There is also a challenge to balance the requirements of maintaining sufficient spatial resolution below $1R_e$, as well as reaching $>2R_e$ which is a requirement for reaching the turn-over in the rotation curves of disc galaxies (e.g. for the Tully–Fisher analysis). Separate samples within the same survey area that can be observed concurrently may be the most natural solution to this problem. Further discussion of the detailed sample selection for a large SAMI galaxy survey is deferred to a future paper.

3 THE SYDNEY-AAO MULTI-OBJECT INTEGRAL FIELD SPECTROGRAPH (SAMI)

With a view to providing the first on-telescope demonstration of hexabundle technology, the Australian Astronomical Observatory (AAO) and the University of Sydney have collaborated on the development of the SAMI instrument for the 3.9-m Anglo-Australian Telescope (AAT). SAMI uses 13×61-core hexabundles that are mounted on a plug plate at the 1-degree FoV triplet corrector top-end focus of the AAT. At f/3.4, with 105 μm core diameter fibres, each hexabundle samples a 14.9 arcsec diameter field at 1.6 arcsec per fibre core. At the output end, a total of 13 V-groove slit blocks are mounted at the slit of the AAT's AAOmega spectrograph [Sharp et al. (2006); also see Section 3.7]. Each slit block includes 63 fibres (all the fibres from one hexabundle plus two fibres for sky subtraction). A fusion-spliced ribbonized fibre cable of length ∼42 m joins the two instrument ends together. A near real-time data pipeline, based on the 2DFDR code (Croom, Saunders & Heald 2004b; Sharp & Birchall 2010), has been written to reduce the data.

The following subsections describe the instrument requirements, fibre cable, the hexabundles, the prime focus unit, the SAMI field plates, the AAOmega spectrograph, the instrument control and data reduction software.

3.1 Instrument requirements

The SAMI instrument was designed to be a technology demonstrator and to carry out significant science programmes. As a result, the final instrument design is influenced by a mix of scientific and technical constraints. A key constraint was to develop the system on a rapid time-scale, which naturally led to the use of the plug-plate system and the already available AAOmega spectrograph. The flexibility of AAOmega, with a range of resolutions and wavelength settings, also enables a variety of science.

In order to make a substantial advance over previous facilities, the multiplex of the system had to be at least an order of magnitude better than previous monolithic IFUs (i.e. SAMI required at least $\simeq$10 IFUs). The median optical seeing at the AAT is $\simeq$1.5 arcsec, so the fibre cores were approximately matched to this (1.6 arcsec diameter). Although undersampling the seeing, this is generally preferable to having smaller core sizes for a number of reasons: (i) larger fibre cores provide more independent resolution elements, (ii) smaller fibre cores will lead to data being read-noise limited in the blue, (iii) larger fibre cores provide better surface brightness sensitivity, (iv) larger fibre cores allow higher fill factors, given a fixed minimum fibre cladding (i.e. 5 μm in our case) and (v) critical sampling of the seeing can still be achieved with dithered exposures.

Given the above, the final key instrument design decision was the number of fibres per IFU. The choice of 61 fibres per IFU was made largely on the basis of the known capability to manufacture such bundles. However, this number of fibres also matches other requirements. Larger numbers of fibres per bundle would have restricted the multiplex given the fixed AAOmega slit length, and the chosen 15 arcsec IFU diameter provides a good match to the scale length of galaxies in local samples chosen to match the surface density of SAMI IFUs within the 1-degree diameter FoV (see Section 2.7). If designed for a single experiment, one option would have been to have a variety of bundle sizes to match the specific galaxy size distribution of the target sample. However, for ease of manufacture, and to maintain multiplex and flexibility, we chose to have all the IFUs the same size.

3.2 Fibre cable

SAMI is mounted at prime focus on the AAT and feeds the AAOmega spectrograph located in the Coudé room, requiring a fibre cable run of $\sim$42 m. Within the fibre bundle a total of 819 fibres are used: 793 for the hexabundles (13 × 61 fibres), and 26 for the sky fibres. The hexabundles were each supplied with a fibre pigtail length of 1 m encased in a reinforced furcation tube. Each of the hexabundle and sky fibres were fusion spliced on to a fibre of length $\sim$42 m that is terminated in a V-groove block at the spectrograph entrance slit (see Section 3.7). For this fibre run we chose a fibre ribbon cable to minimize the required assembly effort. Each 250 µm thick ribbon contains eight fibres, and eight ribbons are used for each of the 13 units (one hexabundle plus two sky fibres). To minimize losses in the splicing process, and because of its ready availability, we matched the ribbonized fibre type to that used in the hexabundles (ThorLabs AFS105/125Y).

A 'splice-box' is mounted on the internal wall of the telescope top-end barrel that incorporates 13 closed-cell polyethylene trays to secure and protect the individual splices of each unit. The inputs to this box are the 26 sky fibres [each individually sleeved with reinforced PVC furcation tubing and terminated with SubMiniature version A (SMA) connectors] and the 13 individual hexabundle tubes. The output of this box is the fibre bundle. The bundle is protected during its run (which goes through the top end telescope ring, beside the primary mirror support, and through the declination drive axis to the Coudé room) by an inner covering of braided cable sleeving and an outer double-split nylon conduit giving light-weight yet relatively strong protection.

Though the use of ribbonized fibre worked well in terms of handling and assembly, tests showed that ribbonizing caused a loss due to focal ratio degradation (FRD), as discussed in Section 3.4. The fibre type used provides relatively good throughput above 450 nm, though it suffers higher absorption losses in the UV than other fibres more commonly used in astronomical instruments. The current fibre cable described in this paper will be replaced in the first half of 2012 to provide much improved blue throughput.

3.3 Hexabundles

Bland-Hawthorn et al. (2011) introduced a new imaging fibre bundle optimized for low-light astronomical applications. The hexabundle incorporates several technological innovations in order to achieve a high fill factor. A primary goal of the hexabundle design is that the performance of individual multi-mode fibres should be as good as the same fibre in isolation. Consequently, we were forced to

reject an earlier design where the fibre cores were forced into non-circular shapes because the added FRD [numerical aperture (NA) up-conversion] was found to lead to significant light loss (Bryant et al. 2011).

Within each hexabundle, the 61 circular fibres (with NA = 0.22) are lightly fused together and infilled with low-stress glue. The multi-mode fibres have relatively small core diameters of 105 µm. In order to achieve a high filling factor (75 per cent), it was necessary to reduce the cladding to only 5 µm. The length of the fused region is very short ($\approx$30 mm) to minimize cross-talk between the fibre cores. The fibre bundle is held within a reinforced flexible plastic tubing that is both strong and light-weight. The optical head is supported by a stress-relieving sleeve and is inserted into an SMA connector. This is to allow the fibre bundle to be manually attached to the field plate with relative ease. The repeatable positioning accuracy made possible by the SMA connector is much better than a fibre core size.

The use of bare fibre hexabundles directly at the telescope focal plane is the most novel element of our instrument design. There are several advantages to such an arrangement as an alternative to fibre-lenslet coupled IFUs that have been used elsewhere (e.g. Kelz & Roth 2006). First, the hexabundle is fabricated as a one-step process, whereas a fibre-lenslet system requires the fibre bundle to be manufactured and then bonded to the lenslet array(s). Secondly, there are no optical elements required in our hexabundle design. Lenslet or microlens array IFUs require at least two surfaces and more often up to eight surfaces before the fibre face, to adjust for plate scale and to preserve telecentricity of the telescope beam into the fibre. These extra surfaces add to system loss. A trade-off must be made against the potential for extra losses in the hexabundle (e.g. from FRD – see below) and from its lower fill factor. For SAMI, as we are feeding the hexabundles with a fast beam the FRD should be minimized (if used with the appropriate fibre type). Finally, the hexabundle solution offers the opportunity of reduced pitch between IFUs relative to a lenslet solution that must work at a higher magnification.

3.4 Focal ratio degradation and throughput

FRD increases the size of the light cone coming out of a fibre compared to that put in. The worse the FRD, the more light will be lost from the f/3.15 acceptance cone of the AAOmega spectrograph. However, FRD can be partially controlled by minimizing the stresses on the fibres when installing them in the system. An additional loss comes from the throughput of the fibres, which is primarily dependent on the fibre type and length. In this section we determine the performance of the fibre cable and hexabundles by analysing FRD and throughput. As will be seen below, the dominant source of losses is the fibre cable, rather than the hexabundles.

The FRD and throughput were measured for a SAMI hexabundle using an LED source that was fed through Bessel *B* and *R* filters (centred at approximately 435 and 625 nm) and re-imaged to form an f/3.4 beam. This was then input into several hexabundle cores in turn. The output fibres were imaged in the far-field using an SBIG camera. After flat-fielding the images, the centre of each output spot was fitted. Encircled energy (EE) was calculated in concentric circles about the centre position using software packages within IRAF.

We initially compared the performance of a hexabundle alone to the same hexabundle when spliced to the 42 m of ribbonized cable with a slit block attached (hexabundle 15, 'alone' versus 'plus ribbon' in Table 1). For three different cores (numbers 1, 6 and 18; see Fig. 3), the throughput dropped to $\simeq$65 per cent in the red and

Table 1. FRD and throughput results for the SAMI fibres and hexabundles. The bare and ribbonized fibre used is the same AFS fibre as in the hexabundles. Results are shown for the central core (core 1) of hexabundle number 15 before the hexabundle was spliced to the fibre run. Then for core 1 and for two other cores (6 and 18) in the same hexabundle, when the bundle was first spliced to the 42 m of ribbonized cable with slit block attached. Lastly, for the hexabundle with 42 m of ribbonized cable and slit block, but measured after the first SAMI commissioning run, when the ribbonized cables had been packed into a braided cable sleeve and outer nylon conduit. Cores 1 and 18 are on the edges of a ribbonized cable, while core 6 is in the centre of a ribbon. All measurements are based on an f/3.4 input to the hexabundle and f/3.15 output (accepted by AAOmega). The NA up-conversion is the difference between the input and output NA at 90 per cent EE and has an error in each case of ±0.009. The predicted performance is what we expect to achieve when the fibre run has been replaced with a higher throughput fibre (e.g. Polymicro FBP) and the effects of ribbonizing are removed.

| Fibre	Throughput		NA up-conversion	
	Red	Blue	Red	Blue
	per cent	per cent	90 per cent EE	90 per cent EE
Hexabundle 15				
Core 1 alone	96 ± 6	89 ± 5	0.003	0.009
Core 1 plus ribbon	67 ± 7	41 ± 6	0.028	0.037
Core 1 plus ribbon				
After run	44 ± 7	24 ± 6	0.067	0.073
Core 18 plus ribbon	64 ± 8	43 ± 7	0.026	0.034
Core 18 plus ribbon				
After run	37 ± 8	22 ± 7	0.076	0.082
Core 6 plus ribbon	65 ± 8	40 ± 7	0.028	0.037
Core 6 plus ribbon				
After run	56 ± 8	32 ± 7	0.037	0.044
Predicted performance	84	62		
With replacement fibre				
42 m bare fibre	78 ± 5	58 ± 5	0.008	0.018
42 m ribbonized	73 ± 5	53 ± 5	0.022	0.031
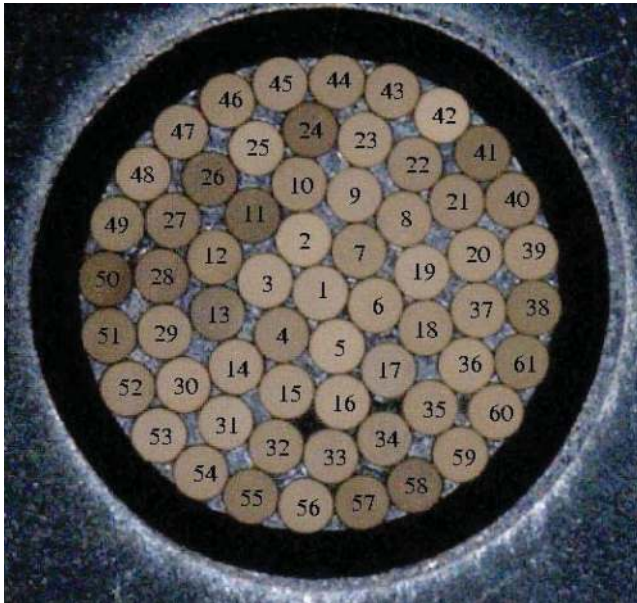
Figure 3. An image of a hexabundle front facet. This shows the 61 optical fibre cores, which have a total active area of diameter 980 μm. Surrounding the fibre cores is a glass ferrule (black ring), which in turn is surrounded by the central steel pin of the SMA connection, which extends beyond the edge of the image.

Figure 4. EE versus NA profiles in *B* band for an input of f/3.4. Larger FRD (or NA up-conversion) shifts the curves to the right. The vertical line marks an output of f/3.15 (into AAOmega). The black curve is the input light curve. The cyan line is the FRD of the hexabundle alone, without the ribbonized cable. The green, red and blue *solid* lines that are nearly on top of each other are the curves for cores 1, 6 and 18 once spliced to the ribbonized 42 m cable and attached to the slit block, but before being put into the cable sleeve and outer nylon conduit (errors are ±0.006 in NA). The dashed curves (with errors of ±0.0065) are for fibres 6, 1 and 18 (same colours as above), after the ribbonized fibre was put into the cable sleeve and outer nylon conduit and had been transported to the telescope, installed and used for the first commissioning run.

41 per cent in the blue with the addition of the ribbonized cable plus slit block. Fig. 4 and Table 1 show that this drop is identified with a significant increase in FRD, with the NA up-conversion (at 90 per cent EE) for the hexabundle with ribbonized fibre measured to be
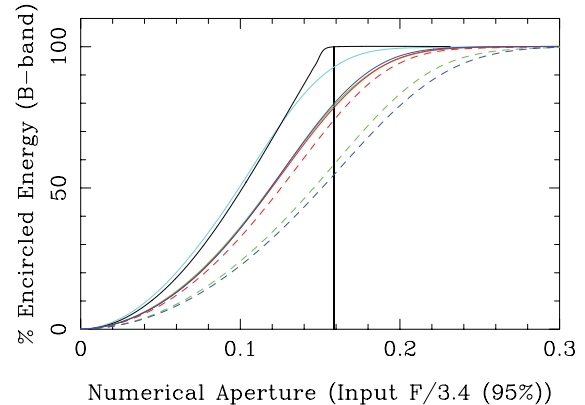
significantly worse than for the hexabundle alone. The end finish on the bundle alone was a cleave, but the measurement through the ribbonized fibre and slit block had the advantage of a polished end finish which should improve the FRD, so the FRD introduced

by the ribbonized fibre may be a little worse than these numbers indicate.

In order to differentiate between the effect of the 42 m of fibre and the ribbonizing, we separately compared bare and ribbonized fibre throughputs (Table 1, lower panel). This was done by measuring the throughput from 10 m of bare fibre of the same type as used in the hexabundles and ribbonized fibre (AFS105/125Y). The 10 m was then cut, spliced together and measured to give the splice loss. Then the splice was cut and an additional 42 m was spliced in place. This was then cut out and 42 m of ribbonized cable was spliced in instead. The throughput could then be compared for the bare and ribbonized cable after accounting for the initial 10 m. Having the initial fibre in place meant that the FRD results for the bare and ribbonized fibre were not affected by coupling into the fibre or end finishing effects as these remained the same for both tests. Variations in throughput due to the different splices have been taken into account in the errors. Table 1 shows that while the bare fibre results will include end effects, the ribbonizing of the fibres results in significantly worse FRD. The bulk of the loss in throughput is due to the length of fibre (78 per cent throughput in red and 58 per cent in blue), however the FRD from ribbonizing results in less of that light coming out within the f/3.15 acceptance cone of the spectrograph.

Once the hexabundles were spliced to the ribbonized cable and slit blocks ('plus ribbon' in Table 1), the throughput was lower than that measured for the 42 m of ribbonized cable alone. This is due to an increase in the FRD above that of the ribbonizing. The small additional FRD is therefore due to the hexabundle and slit block. Mechanical stress on the fibres when mounted in the slit block can increase the FRD (see e.g. Oliveira, de Oliveira & dos Santos 2005), and hence decrease the throughput within f/3.15.

During the commissioning run it was noted from AAOmega images that the throughput of the fibres on the outer edge of each ribbonized cable was lower than that of the fibres in the centre of a ribbonized cable. Therefore, two fibres on the edge of a ribbon and one in the centre of a ribbon were tested after SAMI had been taken off the telescope. The testing method was identical to that described above, and the three fibres tested were among the same fibres from the bundle that was tested before the SAMI commissioning run. In Fig. 4 and Table 1 it is notable that while the fibres had similar performance before commissioning (see 'core plus ribbon' in the table), after commissioning (see 'core plus ribbon after run') the FRD was substantially worse for the two fibres on the edge of a ribbon (fibres 1 and 18). Meanwhile, the fibre in the centre of the ribbon (fibre 6) showed only a small increase in NA up-conversion compared to the previous results. The throughput within f/3.15 for the cores on the edge of a ribbon decreased from 64–67 and 41–43 per cent (red and blue, respectively) before the SAMI installation to 37–44 and 22–24 per cent after the SAMI commissioning run. However, the hexabundle core in the centre of a ribbon (core 6) had a comparatively higher throughput of 56 per cent and 32 per cent.

We believe that the increased FRD for the edge fibres is due to stresses in the ribbonized cable when it was fed into the braided cable sleeving and outer nylon conduit that protects the fibre run. As the fibre bundle was moved during transport, installation and commissioning, the ribbonized bands could be bent in all directions, in which case the edge fibres come under more stress than the centre.

The throughput of SAMI will soon be significantly improved by the replacement of the fibre run. The loss due to the fibre length will be reduced, particularly in the blue, by using a different type of fibre. The fibres being considered will result in up to 14 per cent higher throughput at the blue end of the spectrum. In addition, if
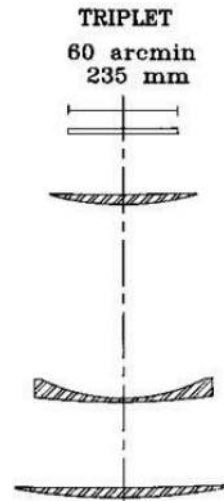
Figure 5. Schematic of AAT prime focus triplet corrector.

the effects of ribbonizing and FRD stresses from the ribbonized cable are removed, the throughput would further increase by up to ~27 per cent, perhaps doubling the current blue throughput. An alternative protection will be required for the 42 m fibre run, and that may introduce some FRD losses, but it is being designed to have less of an effect than the ribbonizing.

3.5 Prime focus unit

Within the AAT prime-focus top-end, the triplet corrector and the Prime Focus Camera were refurbished for the SAMI instrument. Originally built for the commissioning of the AAT in the early 1970s, they provide a 1-degree FoV with a plate scale of 15.2 arcsec mm^{-1}. With 61×105 μm cores, this provides a 15 arcsec diameter FoV for each hexabundle and a sampling of 1.6 arcsec per fibre core (see Fig. 5).

With a total of 39 fibre positions in each field (26 sky positions and 13 object positions), we chose to use a plug-plate assembly rather than a robotic positioning system, as the operational overhead and down-time between fields for reconfiguration are both relatively low, particularly as we are targeting long (~2-h) integrations and have a connectorized fibre system.

The SAMI plug plates are pre-drilled 3-mm-thick brass discs with through-holes at each object/sky location. Each hexabundle and sky fibre is terminated in a SMA screw-thread fibre connector. A mating connector is installed in each plug plate at each position. Two galaxy fields (i.e. 26 objects) are pre-drilled on the plate along with a set of 26 blank-sky locations common to both galaxy fields. For the proposed integration time of 2 hours per field, this means that two plates (and one plate exchange) are required on each observing night. The down-time between fields recorded during the initial commissioning run was less than 30 min. Further investigation found that it was possible to include four fields per plate, so that no plate exchange is required during the night.

The plug plates are installed within an assembly that is kinematically mounted to the Prime Focus Camera (see Fig. 6). Due to the relatively large FoV of each hexabundle, there is not a strict requirement on the positioning accuracy of each hexabundle central fibre. However, we aim to reach a total positional accuracy of half the core diameter of a single fibre (i.e. 0.8 arcsec). The accuracy achieved is determined by several factors that include: the hexabundle concentricity; the connector concentricity; the plug-plate
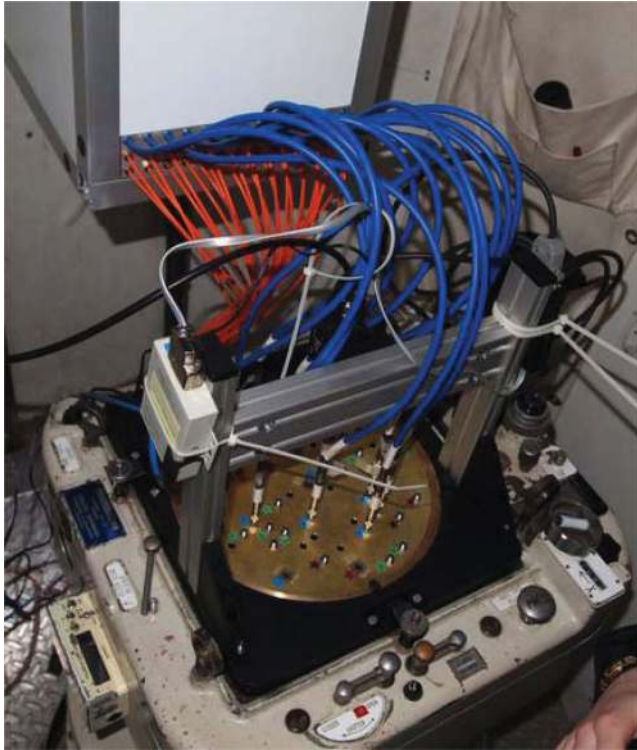
Figure 6. The SAMI plug-plate assembly unit mounted on to the Prime Focus Camera. The white 'splice box' (top) connects the blue hexabundles and orange sky fibres from the brass plug plate to the fibre bundle. The cross-bar above the field plate provides a location to mount the guide camera, which images the hole in the middle of the plate.

machining accuracy and the plug-plate thermal expansion. These factors are all controllable to within much less than a fibre core. Additional position errors are introduced via (i) a rotation offset, which is corrected via a fine-thread micrometer rotation adjustment between the plug-plate assembly and the Prime Focus Camera, (ii) an asymmetric radial error arising from an *x*–*y* offset of the plug plate from the telescope optical axis, for which the tolerances are quite large, and (iii) a symmetric radial error arising from an in-correct plate scale, which can be corrected after measurement by producing a new distortion map.

For image reconstruction it is important that the rotational align-ment of each hexabundle is known. Because the SMA connec-tor has no rotation adjustment capability and is not rotationally keyed, the orientation of the hexabundles was determined by eye as they were inserted into the plug plate. Laboratory and on-sky tests demonstrated that an accuracy of less than half a core in the outer hexabundle ring ($<10°$) was possible with this technique. The SMA connectors will shortly be replaced by keyed FC connectors to eliminate this limitation.

For acquisition and guiding, we use a CCD camera mounted on a gantry above the plug plate that views (via an optical relay) the central region of the field through a hole in the plate. This camera (an 800×600 pixel Watec #120N) provides a video output signal that can be integrated from frame rate up to $\sim$10 s and is compatible with the existing AAT control system guiding software. It reaches $\sim$14th magnitude over a sky FoV of 150 arcsec diameter (providing a sufficiently high sky coverage factor for most galactic latitudes) and has a sampling of 0.3 arcsec pixel^{-1}.

3.6 Field plate manufacture

Using the manual plug-plate method for positioning the hexabundles in SAMI presents a number of challenges for the field allocation and plate manufacturing. Here we describe the SAMI field configuration methodology.

The plates are manufactured using brass of thickness 3 mm and approximate diameter 240 mm (corresponding to the 1-degree FoV). The fibre connectors have an assigned footprint of 15 mm to allow access for installation and removal. The instrument uses two distinct physical plate types: science and calibration. Each plate is config-ured with multiple stacked fields for efficiency gains. There is a central 10 mm hole in each plate for the guide camera to image a sky region of diameter $\sim$150 arcsec.

The science plates consist of two stacked galaxy fields each with 13 galaxy targets for the IFUs and about five field alignment stars, also targeted with IFUs. The field alignment stars did not share the same field centre as the galaxy targets. During commissioning, when the plate was first observed, IFUs were positioned at the location of the alignment stars in order to check for consistent rotation and plate scale between each plate. Once confirmed, the IFUs were re-allocated to galaxy targets and the telescope moved to the science field centre. Each plate also contained 26 sky fibre positions shared between the two galaxy fields. The science plate is configured for consecutive fields requiring only the re-positioning of the 13 IFUs on to new galaxy targets. Each science plate then has a total of $\sim$62 drilled holes for the installation of the SMA fibre connectors (with a minimum separation of 15 mm). The astrometric calibration plates were constructed in a similar way, but in that case each plate contained four overlapping fields and four visual alignment fields.

The process for generating a single field was as follows.

(i) For each RA region, convert the RA and Dec. coordinates to angular distance coordinates and calculate the pairwise distance matrix of all targets.

(ii) Iterate over each target using the distance matrix to extract targets within a $0°.5$ radius and to remove targets with separations <15 mm ($\sim$228 arcsec).

(iii) Count the number of targets and identify this as a candidate field if the total is equal to or greater than N, where N is the number of sources required; $N = 14$ for astrometric calibration fields (13 IFU targets plus central guide star), $N = 3$ for visual alignment fields (two visual targets and a central guide star) and $N = 13$ for science fields.

(iv) For a candidate field, save the data and assign the field to that RA region; eliminate the field's allocated objects from the list of potential targets (in order to produce fields with unique sets of targets).

Once individual fields were defined, multiple fields were stacked on a single plate (e.g. for science fields the plates contain 2×13 galaxies plus 2×5 alignment fields; for astrometric calibration fields the plates contain 4×13 calibration targets plus 4×2 visual alignment fields). Fields were grouped into RA regions (typically of size $20°$ in RA) based on observation times. The RA regions were ordered based on the best observing time for each region (i.e. the time of the lowest airmass). Then fields were tested in turn to see that the allocated targets did not overlap, so that they could be stacked on to an individual plate. The priorities of the targets in each science field are summed to give a figure of merit for all possible plate permutations. The permutations can be filtered for field duplicates and sorted by merit.
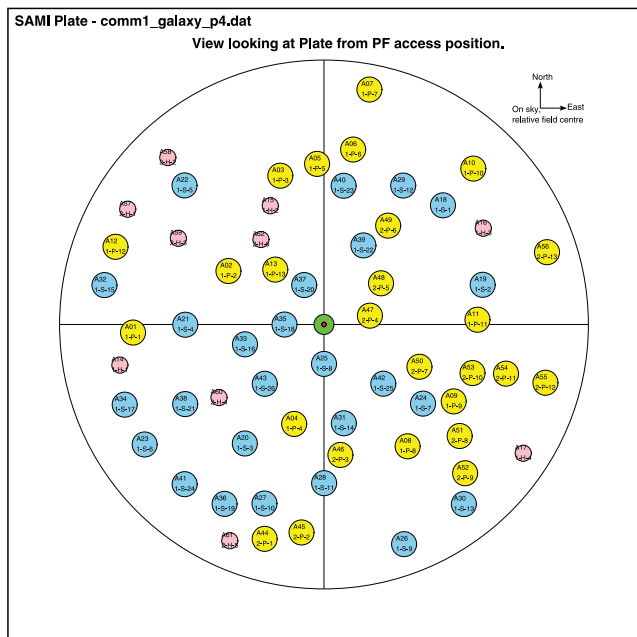
Figure 7. Example SAMI science plate schematic showing 2×13 galaxy fields (yellow/orange), 26 common sky fibres (blue), 2×5 field alignment stars (pink) and the central guide window (green).

Once the plate configuration was defined, we determined the 26 sky fibre positions that are shared for each field. This was based on a grid of regularly spaced angular positions relative to the plate centre (e.g. 25×25 grid points over the field), which were then converted to RA and Dec. given each field centre, and to relative plate coordinates in microns (the same for each field). Sky fibre grid locations were eliminated if they overlapped with the science targets in plate coordinates. SuperCOSMOS images (Hambly et al. 2001) were examined at the RA and Dec. of each remaining sky grid position for each field and if no source was found within a 24 arcsec window then the sky position was accepted. From these remaining candidates, 26 sky fibre locations were then selected for targeting.

For each stacked field, we then determined suitable guide stars ($V < 14$) in the central 150 arcsec FoV using the Aladin sky atlas (http://aladin.u-strasbg.fr/) to search the USNO-B1 catalogue and examine Digital Sky Survey (DSS) images.

After the above process, we take the entire set of target positions in RA and Dec. and convert them to accurate plate X–Y coordinates using the optical distortion model of the prime focus corrector and the differential atmospheric refraction at the expected time of observation. These X–Y positions were then converted to mechanical drawings (with temperature compensation to allow for the difference between the average day-time drilling temperature and the average night-time observing temperature), and these were the input to a CNC machine for drilling the plates to the required specification. A schematic of a galaxy field plate is shown in Fig. 7.

3.7 AAOmega spectrograph

AAOmega (Sharp et al. 2006) is a fibre spectrograph designed for use with the 2dF robotic fibre positioner on the AAT. It has a double-beam Schmidt design that allows for optimized performance in the red and blue simultaneously. Volume-phase holographic (VPH)

gratings are employed to give high throughput. There are a range of gratings available, giving resolutions from ~1700 to ~13 000 for the SAMI fibres (105 µm diameter). There is a choice of two dichroics that split the light and direct it to the blue and red cameras; one dichroic has a cut-off wavelength of 570 nm and a second at 670 nm. The detectors are 2k × 4k E2V devices with the short axis in the wavelength direction and the long axis in the spatial direction.

For operation with the 2dF top-end fibre feed, the AAOmega slit is populated with 392 fibres that each have 140 µm cores, projecting to ~3.4 pixels on the detector, with a core-to-core pitch of 10 pixels. AAOmega is also fed by the SPIRAL IFU used at the AAT Cassegrain focus. SPIRAL has a 16 × 32 rectangular lenslet array, with a sampling of 0.7 arcsec. The 512 SPIRAL fibres have 85 µm core diameters, which project to ~2.4 pixels on the detector. The fibre cores are separated on the slit by a pitch of 140 µm.

For SAMI we have matched the fibre core-to-pitch ratio of SPIRAL, which is $85/140 = 0.61$. This is more closely packed than used for 2dF, but has proven sufficient with SPIRAL for the minimization of crosstalk between fibres using an optimal extraction methodology described by Sharp & Birchall (2010). The SAMI fibre pitch on the slit is 170 µm, giving a core-to-pitch ratio of $105/170 = 0.62$. This pitch then defines the maximum number of hexabundles (13) that will fit along the concave AAOmega slit while allowing 26 individual sky fibres to also be positioned on the slit.

For convenience of manufacture and assembly, each hexabundle and sky fibre pair is fed to an individual silica V-groove slitlet. The mapping is such that the central core is in the middle of the slit. The outward spiral numbering of the hexabundle cores corresponds to odd and even outwardly alternating fibres in the slitlet, with the sky fibres being the outermost fibres on the slitlet. This arrangement maximizes the number of adjacent hexabundle cores that are also adjacent on the detector and minimizes cross-contamination between sky and adjacent object spectra.

The AAOmega slit is mounted on a rotating mechanism that allows four different slits to be positioned in the beam of the spectrograph. This is used during operation of 2dF, when one of the two fields is being observed while the other is being re-configured by the robot. The SAMI slit is located at one of the previously spare positions on the AAOmega slit rotator; in the course of normal SAMI operations the slit does not move.

3.8 Control software

SAMI uses an adaption of the 2dF/AAOmega control software (Smith et al. 2004). This software has significant flexibility and had been successfully evolved through various changes since it was originally commissioned with 2dF in 1996. As part of the implementation of AAOmega in 2006, the software was modified to support the SPIRAL IFU feed to AAOmega. This operational mode did not use the fibre positioner and atmospheric dispersion corrector (ADC) of the 2dF top-end, and as a result was a good starting point for SAMI. A number of minor modifications were required to the software to support this additional mode of operation.

The 2dF/AAOmega software inserts a large binary table into the CCD data files to fully describe the location and status of each of the fibres. This table differs significantly from versions implemented for SPIRAL and 2dF. A component of the software (the Fibre To FITS program) is used to build this table, and a new version of this program was required for SAMI. It reads a file describing the allocation of objects to IFUs and sky fibres. The software combines this with the telescope pointing information and information from files containing the measured positions of each fibre in each IFU to

determine the actual location of each fibre on the sky. As a result, a EURO-3D compliant (Kissler-Patig et al. 2004) binary table can be generated and World Coordinate System (WCS) information given for each fibre. Extra information in the table is provided to ensure every fibre is fully traceable, and that its position and the origins of its position are well defined.

It is important that fields be observed sufficiently close to the time planned, and for which the plug plate was drilled. Otherwise changes in airmass can cause some objects to be poorly acquired, largely due to differential atmospheric refraction across the FoV. To assist in the decision whether to observe a given plate, the control software displays the error between the drilled hole and the current object sky position for each of the 13 IFU probes at the beginning of each exposure.

3.9 Data reduction software

Data reduction for SAMI is performed using the 2DFDR data reduction pipeline (Croom et al. 2004b; Sharp & Birchall 2010) originally written for the 2dF instrument and then modified for use with the AAOmega spectrograph. This provides fully automated reduction of flat-fields, arcs and object frames, including spectral extraction, wavelength calibration and sky subtraction. The code is run from a fully configurable GUI which allows user control of the algorithms used. The main modifications required for SAMI were a revised algorithm to accurately map the fibre locations across the detector (the 'tramline map') and routines to read new elements of the FITS binary table in the data frames. 2DFDR is sufficiently fast that data can be reduced in real time, a feature that is of particular value during commissioning of an instrument.

The 2DFDR pipeline generates extracted, flat-fielded, wavelength-calibrated, throughput-normalized and sky-subtracted spectra. The data product is a 2D image containing each of the fully reduced 1D spectra, together with a variance array and binary table (see Section 3.8). To allow fast reconstruction of 3D data cubes and first-pass science analysis, we have developed a suite of python-based routines which allow us to: (i) construct and write full data cubes for individual IFUs; (ii) view all 13 reconstructed IFU images collapsed over a user-specified wavelength range; (iii) calculate the centroid of a source within the IFU field; (iv) calculate the offset in arcsec between the source and the centre of the IFU; (v) extract summed spectra for an entire IFU or view individual spaxel spectra and (vi) fit emission lines and construct kinematic maps on the fly.

As an aid to the development of the data reduction pipeline, an instrument data simulator was used. This was based on the simulator used for the new High Efficiency and Resolution Multi-Element Spectrograph (HERMES) being developed for the AAT (Goodwin et al. 2010), but modified to simulate SAMI detector images. This was of particular value in developing the algorithm required to extract the fibre spectra from the 2D image.

3.10 Hardware upgrades

The current system, as described above, performs well (see results below), but substantial improvements can be made in performance and usability. To this end a new fibre cable will replace the current one in the first half of 2012. This will substantially improve the system throughput, particularly at wavelengths <4500 Å. The new fibres will be housed in a low stress cable to further improve throughput by substantially reducing FRD. A third planned modification will be to use a different form of connector for the hexabundles. While providing accurate alignment in the x and y, the current

SMA connectors do not allow easy rotational alignment. The SMA connectors will be replaced with a keyed connector such as the FC type.

4 COMMISSIONING OBSERVATIONS

4.1 Stellar target selection

The astrometric calibration plates consist of four stacked stellar fields ($V_T < 10$ mag), each having 13 IFUs for distortion mapping and alignment refinement as well as four stacked bright stellar fields ($V_T < 6.5$ mag) each with at least two stars for initial visual alignment. The calibration plate field uses a centred guide star located at the field centre.

The calibration plates are derived from the stellar data contained within the Tycho-I Reference Catalogue (TRC; Hog et al. 1998). We trimmed the catalogue on position (Dec. < 20°) and magnitude ($V_T < 6.5$ for visual alignment fields, $V_T < 10$ for calibration fields) for a number of observable RA regions.

4.2 Galaxy target selection

The targets for the commissioning were selected to test the full capability of SAMI, subject to the following criteria.

(i) The density of targets on the sky exceeded the 13 hexabundle units available in the 1-degree field of SAMI.

(ii) The targets were of sufficient angular size to fill the 15 arcsec aperture of each fibre bundle.

(iii) Galaxy surface brightnesses (in either emission lines or continuum) were likely to yield S/N > 3 in the outermost fibres of each bundle in a ∼2-h integration.

We decided to select commissioning targets from a wide cross-section of galaxy spectral types to better constrain the performance of the instrument across a range of future scientific applications.

The target input catalogue was drawn from the 6dFGS (Jones et al. 2004, 2005, 2009), which itself was selected from the Two-Micron All-Sky Survey Extended Source Catalogue (2MASS XSC; Jarrett et al. 2000). The 6dFGS catalogue contains 125 071 red-shifted southern galaxies ($|b| > 10°$) selected to $K \leq 12.65$, $H \leq 12.95$, $J \leq 13.75$, $r_F \leq 15.60$ and $b_J \leq 16.75$. The median redshift of the sample is $z = 0.05$. Apparent galaxy sizes are taken from the 2MASS XSC.

The mean density of 6dFGS galaxies is ∼7 deg^{-2}, substantially lower than the ∼19 deg^{-2} IFU density of SAMI. However, the low-redshift nature of the sample means that 6dFGS target densities vary considerably over the sky, and in the densest regions, 6dFGS target densities exceed the IFU density of SAMI. By careful pre-selection of dense regions we ensured that all 13 hexabundles were filled for every field. Nine dense regions (each of diameter 8°) were selected over a range of hour angle and declination to provide 4086 potential targets for the final allocation of SAMI fields and IFUs.

Targets were ranked on a scale from 1 (lowest priority) to 9 (highest priority) that was used to weight the targets for hexabundle allocation and field placement. Targets were given a greater relative weighting if they had: (i) large angular size; (ii) prominent spectral emission lines; or (iii) a spectrum typical of an early-type galaxy, with high S/N.

The angular sizes used in criterion (i) were 2MASS J-band half-light radii. Galaxies were divided into those with apparent radial sizes $r > 10$ arcsec ($\log r > 1.0$), those with $5 < r \leq 10$ arcsec ($0.7 < \log r \leq 1.0$), those with $4.46 < r \leq 5$ arcsec ($0.65 < \log r$

Table 2. Priorities used in allocating targets for the SAMI commissioning observations (9 is the highest priority and 1 is the lowest).

Priority	Input sample	Spectral criterion	Radial size range	Targets
9	6dFGS main	Strong emission lines	$r > 10$ arcsec	100
8	6dFGS main	Strong emission lines	$5 < r \leq 10$ arcsec	748
7	6dFGS-v	High S/N early-type	$r > 10$ arcsec	28
6	6dFGS-v	High S/N early-type	$5 < r \leq 10$ arcsec	152
5	6dFGS main	Strong emission lines	$4.46 < r \leq 5$ arcsec	107
4	6dFGS-v	High S/N early-type	$4.46 < r \leq 5$ arcsec	202
3	6dFGS-v	High S/N early-type	$r \leq 4.46$ arcsec	216
2	6dFGS main	Strong emission lines	$r \leq 5$ arcsec	298
1	6dFGS main	All others remaining	All others remaining	2235
			Total	4086

≤ 0.7), and the smallest ones that remained, with $r \leq 4.46$ arcsec ($\log r \leq 0.65$). These divisions were chosen to differentiate between those galaxies most closely matched to the hexabundle aperture size (with galaxy diameters 10–20 arcsec), and those outside this range. For the purpose of commissioning, the largest galaxies were also given high priority to extend the range of test subjects.

Criterion (ii) was based on matches to the emission-line galaxy spectral templates used during the 6dFGS cross-correlation redshifting procedure (see Jones et al. 2004). Note that it is not a complete sample, as spiral galaxies which are dominated by their bulge on the scale of the 6dFGS fibre aperture (6.7 arcsec diameter) may not exhibit substantial emission lines in their 6dF spectrum.

Criterion (iii) was populated by the 6dFGS velocity catalogue (6dFGS-v; Campbell 2009; Springob et al. 2011), a high S/N (>10 per pixel in the 6dFGS spectrum) subsample of 11 288 early-type galaxies.

Selecting the target sample in this way ensured that the performance of SAMI would be gauged across a broad range of galaxy types, while also maximizing size and surface brightness considerations, where possible. Table 2 summarizes the selection criteria applied to each of the priority assignments, and the total number of available targets in each case.

4.3 Observations

The first commissioning observations were carried out on the nights of 2011 July 1–4 at the AAT. The primary aims were to test the alignment and astrometry of the plug-plate and hexabundle units, estimate system throughput, and examine the reliability and robustness of the instrument. The secondary goal was to obtain the first galaxy IFU observations with SAMI to test data quality and determine the accuracy with which physical parameters could be extracted.

The AAOmega spectrograph setup used the 580V grating in the blue arm at a central wavelength of 480 nm, covering the wavelength range from 370 to 570 nm (the latter set by dichroic that splits the light between the red and blue arms of AAOmega). With the 105 μm fibre cores of SAMI, the 580V grating provides a spectral resolution of $R = 1730$ [or 173 km s^{-1} full width at half-maximum (FWHM)]. The dispersion is 0.103 nm pixel^{-1}. This wavelength range is ideal for measuring a wide range of spectral features in the blue parts of galaxy spectra at low redshifts ($z \sim 0.05$), such as the D4000 break, [O III] emission, various hydrogen Balmer lines and Mg b. In the red arm, the key spectral features are the Hα, [N II] and [S II] emission lines. As these are all located in a relatively narrow wavelength range (and the target redshift range is small), it is possible to observe all of these features using the higher resolution 1000R grating.

This was set to have a central wavelength of 680 nm, providing a spectral range from 625 to 735 nm. The spectral resolution in the red arm is $R = 4500$ (or 67 km s^{-1} FWHM), with a dispersion of 0.057 nm pixel^{-1}.

The first observations used astrometric calibration plates to measure the accuracy of IFU placement, including checks of rotation, plate-scale and distortion. An initial correction for rotation was applied by one of us (SR) observing a small number of bright ($V_T < 6.5$) stars by eye from within the AAT prime focus unit, using calibration holes drilled in the plate at the position of the stars. The stars were aligned to the holes using the rotational adjustment micrometer on the plate holder assembly (Section 3.5). Once this first correction was made, several astrometric calibration fields were observed in order to make precise measurements of the required parameters.

After the astrometric observations where carried out, we targeted a number of standard stars to measure system throughput, and then a galaxy field was observed as part of science verification. During periods of poor weather other tests were carried out, including examination of guide camera flexure and variations in fibre throughput as a function of telescope position. The detailed results of all commissioning observations are presented in Section 5.

5 RESULTS

5.1 Data reduction

All data presented below were reduced using 2DFDR (see Section 3.9). Fibre flat-field frames illuminated by a quartz lamp are reduced first to define the location of the spectra ('tramline map'), and to construct a fibre-flat-field, which all other frames are normalized by. This provides correction of the relative colour response of the fibres, but not total throughput normalization. Extraction of the spectra was carried out using Gaussian fits to the fibre profiles, based on a mean profile shape. Wavelength calibration was via an arc frames using a copper–argon lamp. Throughput calibration of the fibres was carried out either by using twilight sky frames or the strength of night sky emission lines in the object spectra. Once the fibres were flat-fielded, wavelength-calibrated and corrected for relative throughput, sky subtraction was performed. A median sky spectrum was constructed from the 26 sky fibres. This was then subtracted from the object spectra.

The relative throughput of each fibre is shown in Fig. 8. These are normalized to the median throughput, so are distributed about a value of 1. The full range of throughputs is from $\simeq 0.8$ to 1.2. A marked periodic structure is seen every eight fibres (see inset in Fig. 8) which is due to poorer throughput at the edges of each fibre
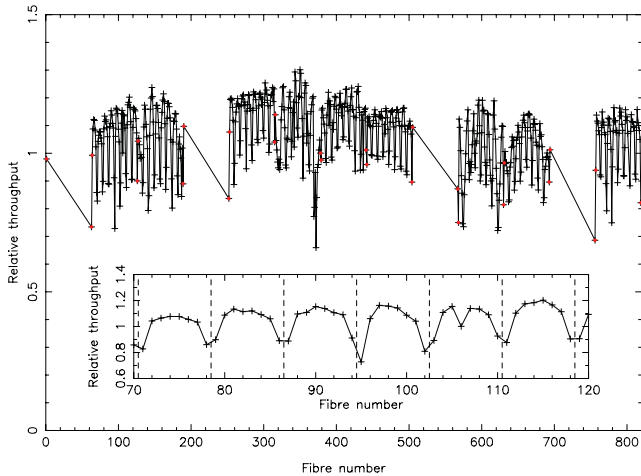
Figure 8. The relative fibre-to-fibre throughput of the hexabundle (crosses) and sky (red circles) fibres as a function of fibre number. Damaged hexabundles are not displayed (including three where the damage is so great the data are not useful, and a fourth where although the throughput is low, there is still reasonable S/N in the fibres). Inset is a small part of the throughput distribution from fibres 70 to 120. Here the periodic decline in throughput at the edges of each fibre ribbon can be seen. The dashed vertical lines break up the fibres into separate fibre ribbons, each containing eight fibres.

ribbon (see Section 3.4) and the relative difference is consistent with the expected throughput loss from FRD measured in the lab-based experiments. The measured rms variation in relative fibre throughput is 0.13; however the uniform throughput away from the ribbon edges suggests that a rebuilt fibre cable not using ribbons would provide much more uniform throughput.

Good throughput calibration and sky subtraction are crucial in obtaining accurate spectroscopy at faint surface brightnesses. Here, we make a preliminary assessment of sky subtraction precision, noting that various upgrades to the data reduction code are still to be implemented. Here we focus on the residual continuum in fibres which were located on blank sky. Minimizing the residual continuum is critical in enabling accurate measurements of stellar population parameters (e.g. age and metallicity) from absorption line indices. The subtraction of night sky emission lines, while also important, can be tackled in a variety of ways, including principle component analysis (Sharp & Parkinson 2010) that can effectively remove emission to the Poisson limit of the data. This approach will be implemented for SAMI data. As the galaxy commissioning targets completely filled the FoV of each hexabundle (see Figs 11 and 16), we used only the sky fibres for this test. It should be noted that the examination of the spectral point spread function (PSF) of sky and hexabundle fibres found no noticeable difference between them, suggesting that a test of only the sky fibres provides a fair assessment of sky subtraction accuracy. Future on-sky tests will confirm this with blank sky observations using the hexabundles. We median filter the sky spectra before and after sky subtraction and then take the ratio of the sum of these median filtered spectra as a measure of the fractional residual sky continuum present. The rms continuum residual about zero is 3.5 per cent, suggesting that in the current data this is the level at which we are accurately subtracting sky continuum. There are a small number (typically ∼2) of sky fibres which perform significantly worse than this (residuals of ∼10 per cent or more). Examination of these fibres showed that (i) they do not demonstrate sky emission line residuals at the same level; and (ii) they tend to be located next to the most badly damaged hexabundle

which projects essentially no light on to the spectrograph CCD. This points to residual scattered light in the spectrograph as the main cause. In particular, the fibre profiles are made up of a Gaussian core and low level, but broad, scattering wings. In regions of the CCD which are fully populated with fibres the scattering wings co-add to form an approximately constant pedestal above the bias level of the detector (when data are sky limited). However, in detector regions without illuminated fibres the background level falls below the pedestal caused by the scattering wings. As a result, fibres on the edge of a blank region have a modified PSF and can be poorly extracted from the data frame. The solution to this is to fit a more complex PSF to the data in the extraction process (e.g. Sharp & Birchall 2010). This will be implemented within the 2dFDR package.

5.2 Astrometry

The AAT Prime Focus triplet corrector distortion is dominated by a pincushion effect. For SAMI, we implemented a model of this using the SLA library routine SLA_PCD (Wallace 1994) and the recommended value of 178.585 for the pincushion coefficient, c. The radial distance in the presence of distortion is given by

$$\rho = r(1 + cr^2) \tag{1}$$

where r is the radial distance from the tangent point. Distances are in units of the projection radius. An analysis of a Zeemax model of the optical system agreed with the previously used model values, to a maximum error of 0.25 arcsec at the field edge. Careful attention was paid to the many orientation and sign issues throughout the software and plate manufacturing process, leading to the first plate being successfully acquired with only a minor rotation correction required.

The AAO implemented a package for calibrating the astrometric models in multi-object spectrographs for the ESO VLT FLAMES instrument (Pasquini et al. 2002) and later for the Subaru Fibre Multi-Object Spectrograph (FMOS) instrument (Kimura et al. 2010). This package, known as FPCAL, can be configured for new instruments by the use of plug-in software components. These components provide the program with an implementation of the optical model and the ability to read details of objects allocated to fibres and the telescope astrometric model parameters from the FITS files generated by the instrument. FPCAL then provides tools to allow fitting of model parameters and the analysis of the results. The user of FPCAL can select either Singular Value Decomposition (SVD) or Powell's method of minimization (e.g. Press, Flannery & Teukolsky 1986) as the fitting algorithm. In practice, these give the same results within noise margins, so the SVD technique is normally chosen as it is faster and provides more information. The appropriate plug-ins to enable us to calibrate SAMI with FPCAL were implemented. FPCAL requires as an additional input the offset necessary to centre each IFU, and software was implemented in python to extract this from the reduced data files. Centroids were calculated using a Gaussian fit to determine the position of calibration stars with respect to the IFU centre.

Observations of three different astrometric calibration fields were made, including fields drilled in different physical plates. An analysis that includes acquisition error, scale, rotation and distortion was performed for each individual field. Sets that combine multiple observations where the stars were offset by ∼2 fibre cores with respect to the IFU centres were used to test the rotation of individual IFUs.

In the initial analysis, results were entirely dominated by minor acquisition and scale issues; the following refers to one typical

observation. An acquisition error of approximately 1.25 arcsec was removed to simplify further analysis. A fit to the scale found a focal length about 20 mm longer than originally presumed; this scale error caused positional errors of up to 1.2 arcsec at the edge of the plate. Removing the scale error resulted in 0.8 arcsec rms residuals. Fitting the pin-cushion distortion parameter and field rotation did not provide a significantly better fit (0.78 arcsec rms residuals). Whilst the change in focal length of 20 mm is larger then expected, this is believed to be due to the power of the triplet corrector, and the actual physical change involved is likely small.

5.3 Throughput

During the SAMI commissioning run two spectrophotometric standards were observed over two nights in several of the individual IFUs. On 2011 July 2 the star LTT6248 was observed in IFU hexabundles 10 and 13 (H#010 and H#013). The first of these observations was used to calculate the overall throughput of the SAMI system including the atmosphere, telescope primary, prime focus corrector, SAMI fibre feed and AAOmega spectrograph. First an integrated spectrum was extracted from the IFU data by summing the spectra in all spatial elements of the IFU. Since the data are under-sampled and the IFU grid is not contiguous, some light is lost between spaxels and a summed spectrum can underestimate the true flux in the star by as much as 10 per cent. This can be avoided by performing a more careful PSF extraction of the star over the relevant FoV, but in this case we used the simpler method and this should be borne in mind for the following results. The summed spectrum was then compared to the tabulated values for the spectrophotometric standard.

The results of this analysis are shown in Figs 9 and 10 for the blue and red arms of the spectrograph, respectively. These throughput curves have not been corrected for telluric features, which are still visible. The curves therefore show the measured throughput of the entire system from atmosphere to detector, including the AAT and the AAOmega spectrograph. Of note is the fact that the throughput falls off quite quickly in the blue arm. This is not ideal but the source of the effect is known. The fibre train for SAMI consists
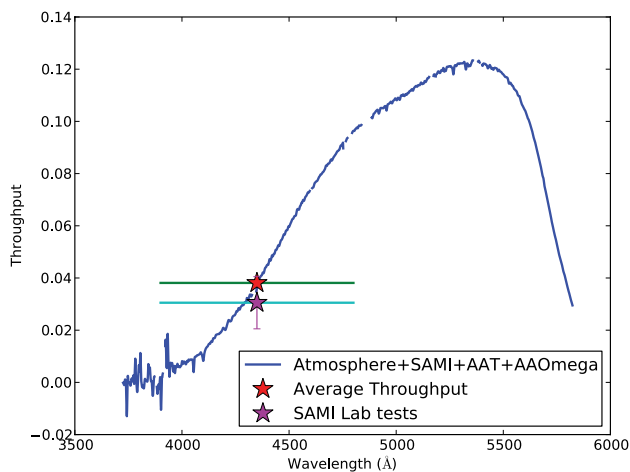

Figure 9. The overall measured throughput for the SAMI system in the blue arm of the AAOmega spectrograph using the 580V grating. The red star shows the measured throughput averaged over the band indicated by the green horizontal line. The purple star shows the lab test estimate, with error bars. The horizontal cyan line indicates the wavelength range over which the laboratory measurements were made. The low throughput in the blue was expected from our choice of fibre for the demonstrator instrument.
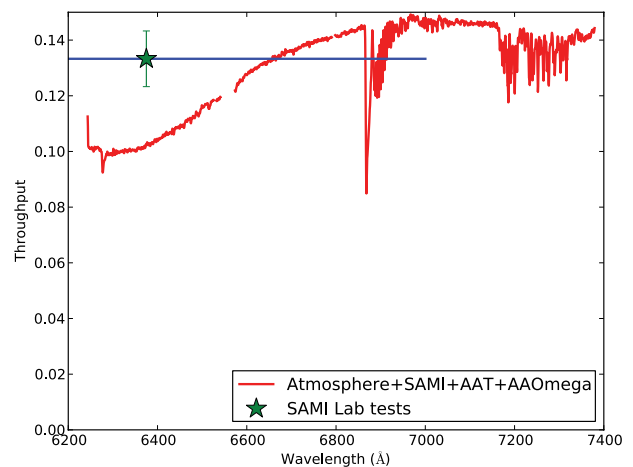
Figure 10. The overall measured throughput for the SAMI system in the red arm of the AAOmega spectrograph using the 1000R grating. The green star shows lab test estimate for the throughput over the *R* band (5750–7000 Å) indicated by the blue horizontal line. The comparison between directly observed and lab-predicted throughputs is approximate as the on-sky observations did not cover the whole of the photometric *R* band.

of ∼42 m of AFS105/125Y fibre matched to the fibre used in the manufacture of the hexabundles themselves. This type of fibre has poorer throughput in the blue than the Polymicro FBP fibre used, for example, in 2dF (Smith et al. 2004).

Throughput values measured from the standard star were compared with the lab-tested throughput from Section 3.4. This is a difficult comparison because the lab tests use Bessel *B*-band and *R*-band filters and the throughput measured from the standard star observations changes rapidly through the bandpass of the Bessel *B*-band filter. The lab tests were corrected for the known throughput in the *B* and *R* bands of the atmosphere (0.72 and 0.89 for *B* and *R*, respectively), telescope including corrector (0.77, 0.80), and spectrograph including CCD (0.17, 0.33). The lab tests have uncertainties due to fibre-to-fibre differences. The data reduction includes fibre-to-fibre throughput corrections for the standard stars, which scales the throughput of each individual fibre to be closer to that of the fibre in the centre of a ribbon. We therefore compare the throughput measured from the observations to core 6 in Table 1. The SAMI standard star images had a steep variation in observed throughput across the *B* band ranging from 26 to 46 per cent (for SAMI only), while the lab-tests found 32 ± 7 per cent. The *R*-band lab measurement is not directly comparable to the on-sky measurement, as the *R*-band filter used in the lab has a peak transmission wavelength outside the range of the AAOmega 1000R grating. However, we show an indicative comparison between direct and lab-based throughput measurements in Fig. 10. The throughput comparisons, while limited by the differences in beam shape and filters used, show that there are no other significant losses in the fully installed system that are not accounted for in the above analysis of throughput.

From the measured throughput of the SAMI system we can calculate the limiting surface brightness for typical observations, assuming photon counting errors. Here we assume 3 h exposure time per field and a dark sky (*V* and *R* band sky brightnesses of 21.5 and 20.8 mag arcsec^{-2}). For an S/N of 5 Å^{-1} the estimated limiting surface brightness is 22.9 and 22.5 mag arcsec^{-2} for the *V* and *R* bands, respectively (on the Vega scale). For a fiducial galaxy survey sample, which is flux limited to $r < 16.5$ and redshift $z < 0.13$,

Table 3. Galaxies observed with SAMI during the July commissioning run. Uncertainties on magnitudes and colours are typically ~0.1 mag.

Hexabundle	RA (J2000)	Dec. (J2000)	Priority	6dFGS ID	Redshift	b_J	$b_J - r_F$	$b_J - K$	Radius[a] (arcsec)	Throughput flag[b]
H#016	19 55 18.8	−54 59 35	1	g1955188-545935	0.019	15.43	1.29	4.68	11.6	Good
H#015	19 55 26.8	−55 09 20	3	g1955268-550920	0.045	16.49	1.43	4.30	3.4	Good
H#005	19 56 51.4	−54 58 37	1	g1956514-545837	0.061	16.65	1.37	4.35	5.2	Bad
H#010	19 56 51.6	−55 19 56	1	g1956516-551956	0.056	16.35	1.23	4.23	5.3	Good
H#004	19 56 56.7	−55 47 30	1	g1956567-554730	0.018	14.67	1.03	3.62	8.1	Good
H#014	19 57 11.2	−55 25 09	1	g1957112-552509	0.059	16.40	1.33	4.41	4.4	Good
H#009	19 57 22.2	−55 08 14	1	g1957222-550814	0.016	15.36	1.25	4.31	10.6	Good
H#011	19 57 33.7	−55 34 41	1	g1957337-553441	0.017	14.45	1.26	4.32	8.1	Good
H#001	19 58 00.3	−55 33 29	1	g1958003-553329	0.056	16.90	1.46	4.55	3.4	Good
H#012	19 58 12.8	−55 40 53	9	g1958128-554053	0.017	15.62	0.16	4.07	14.5	Good
H#006	19 58 29.1	−55 09 13	1	g1958291-550913	0.058	16.14	1.40	4.65	4.9	Bad
H#013	19 58 45.0	−55 35 11	1	g1958450-553511	0.058	16.11	1.24	4.20	5.5	Good
H#002	19 56 17.6	−55 07 11	1	g1956176-550711	0.060	16.96	1.73	3.97	2.4	Bad

[a]*J*-band effective radii from 2MASS XSC.
[b]The 'bad' flag indicates the three hexabundles that were damaged during the run.

these surface brightness limits will allow the current SAMI system to achieve S/N $\geqslant$ 5 at 1 r_e for 80 per cent of galaxies.

5.4 Galaxy observations

One galaxy field with 13 galaxies was observed during the commissioning run. Three 40-min exposures were taken at this pointing on the night of July 2. These were reduced using 2DFDR and stacked, resulting in a total of 2 h integration on this field. A spectrophotometric standard star was observed on the same night as the objects and was reduced in an identical way. The extracted star spectrum was then used to correct the galaxy data for instrument throughput, though the data were not fully flux-calibrated. The details of the 13 target galaxies are given in Table 3.

Fig. 11 shows the 10 galaxies from the observed field that had usable data. The remaining three hexabundles were damaged during
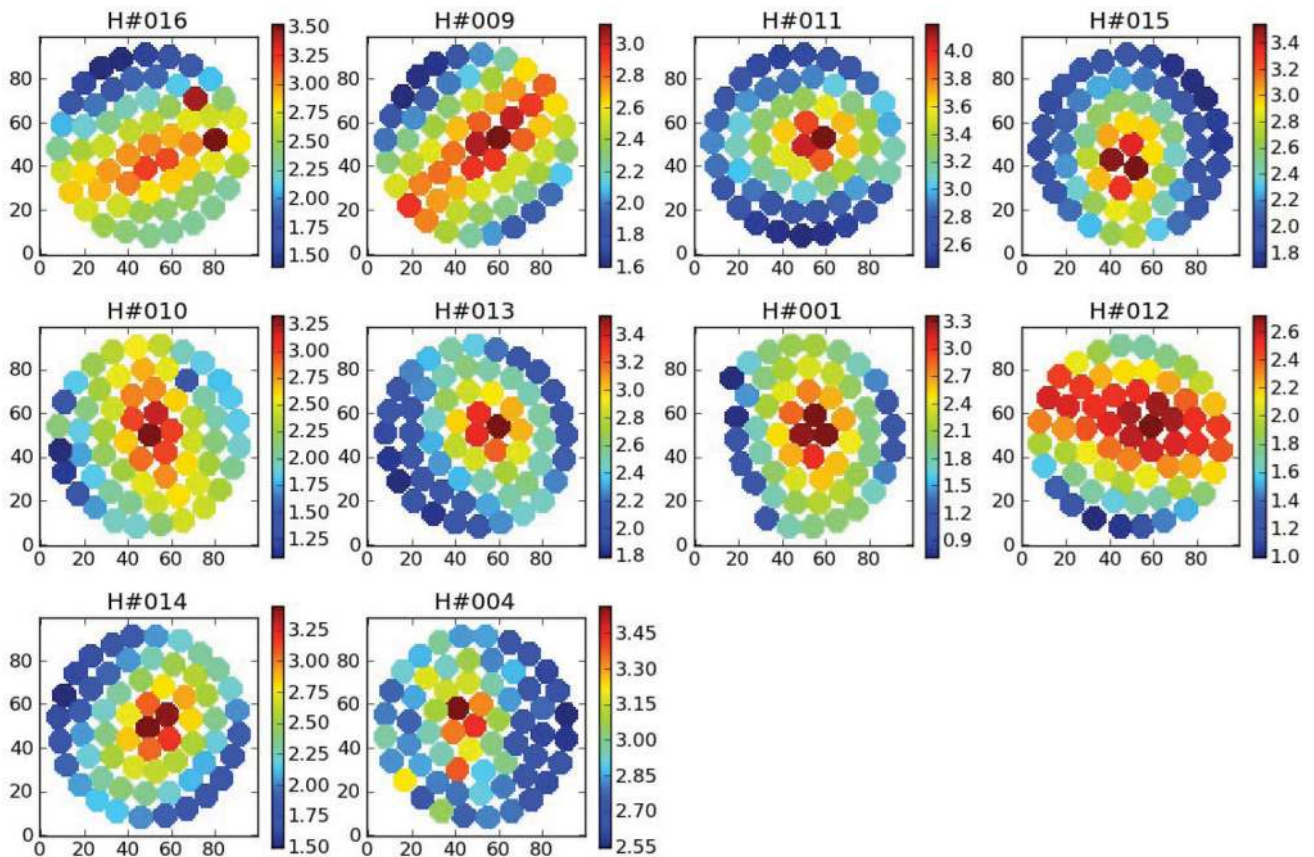

Figure 11. IFU images of the observed SAMI galaxies obtained by summing over the spectrum in each spaxel. The *X* and *Y* positions are in arbitrary pixel coordinates. Each spaxel is represented by a circle with a 10-pixel diameter corresponding to 1.8 arcsec. The colour scales indicate the logarithm of the flux in arbitrary units.
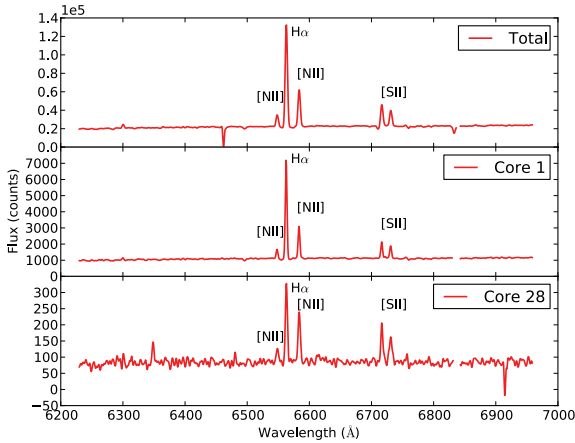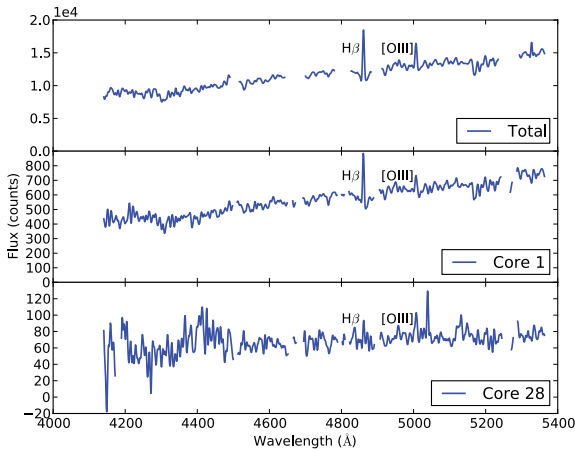
Figure 12. Red spectra for the galaxy observed with bundle H#009. The top plot shows the integrated spectrum converted to rest frame coordinates. The central plot shows the spectrum from core 1 of the hexabundle and the bottom plot shows the spectrum from core 28. The Hα, [N II]λλ6548, 6583 Å and [S II]λλ6716, 6731 Å emission lines are clearly visible.

Figure 13. Blue spectra for the galaxy observed with bundle H#009. The top plot shows the integrated spectrum converted to rest-frame coordinates. The central plot shows the spectrum from core 1 of the hexabundle and the bottom plot shows the spectrum from core 28. The Hβ and [O III]λ5007 Å are clearly visible in the integrated and central spectra but have lower S/N in the outer spectrum. The masked regions in the spectra are due to bad pixels in the AAOmega blue CCD.

commissioning. The images were created by summing over a wide wavelength range (6300–7300 Å in the observed frame); the colour bars indicate the logarithm of the flux in arbitrary units. The discs and bulges of the larger galaxies are readily apparent.

Representative spectra of the galaxy observed in bundle H#009 are shown in Figs 12 and 13. The three spectra in each figure correspond to the integrated spectrum of the galaxy (top panel), the spectrum observed in the central core (core 1; the central panel) and the spectrum observed in an outer core (core 28; the bottom panel). The integrated spectra are simply the sum of all the individual spaxel spectra in a particular IFU. Various emission and absorption features are seen in the galaxy spectra. In the red wavelength range the Hα, [N II]λλ6548, 6583 Å and [S II]λλ6716, 6731 Å emission lines are clearly visible in all three spectra, though with lower S/N in core 28. In the blue wavelength range we see the Hβ and [O III]λ5007 Å emission lines, with an Hβ absorption feature also visible. The data
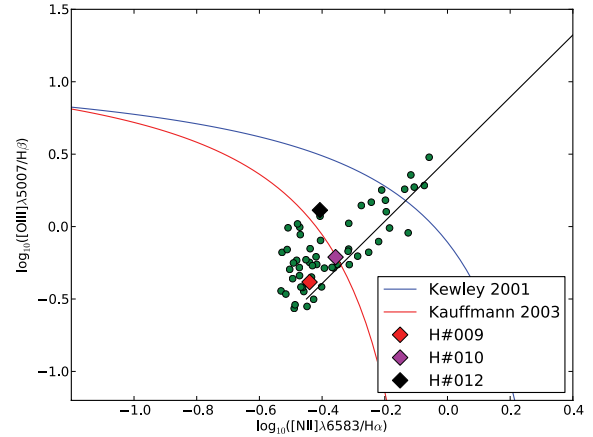
Figure 14. A BPT diagram showing the positions of the three SAMI galaxies for which it was possible to fit all lines. Also shown are the theoretical maximum for star-forming galaxies (blue curve) and the empirical cut-off for star-forming galaxies (red curve); AGN and LINERs are separated, empirically, by the black line (AGN above, LINERs below); see text for details. The green dots show the positions of each of the individual spaxels for the galaxy observed with bundle H#009.

in core 28 have lower S/N than the central core, but still sufficient for analysis.

In examining the results, we first studied the integrated spectrum of each galaxy. Seven galaxies show medium to strong Hα and [N II] emission (along with the [S II] doublet at 6716 and 6731 Å) and three of these also show the Hβ and [O III] lines.

The ratios of these lines are often used to classify objects by means of a so-called BPT diagram (Baldwin, Phillips & Terlevich 1981). Each line was fitted with a Gaussian to measure the line strength. In the case of Hβ, a weak absorption trough was observed in the summed spectra of all three galaxies; this trough was fitted separately and accounted for when calculating the Hβ line strength. Fig. 14 shows the galaxies on a BPT diagram (large diamonds). In Fig. 14 the blue curve shows the theoretical maximum line for star-forming galaxies after Kewley et al. (2001) while the red curve shows the empirical cut-off for star-forming galaxies from Kauffmann et al. (2003). The black line is an empirical line, also from Kauffmann et al. (2003), that separates AGN (above the line) from LINERs (below the line).

The galaxy H#009 (an image of which is shown in the left-hand panel of Fig. 15) was then studied in more detail, using the full spatially resolved set of spectra. The line ratios discussed above were calculated for each individual spaxel in the IFU FoV, yielding spatially resolved line ratio maps, which are shown in the centre and right-hand panels of Fig. 15. There is a systematic spatial trend in both line ratios moving away from the plane of the galaxy's disc. The green circles in Fig. 14 show the line ratios from each spaxel plotted on a BPT diagram. A strong trend is seen in the sense that the spaxels further from the plane of the disc have a harder ionizing mechanism, reflecting the spatial trend seen in the line ratio maps. A single-fibre spectrum of this galaxy would have seen only the central few arcsec of the object and resulted in classification as a normal star-forming galaxy. It is clear from the SAMI results, however, that there is a more interesting story behind this galaxy, which will be discussed in detail in a future paper (Fogarty et al., in preparation).
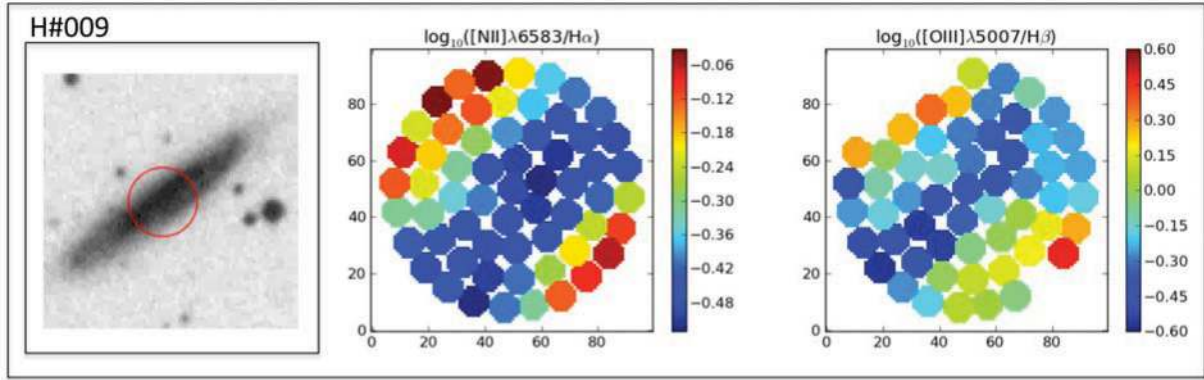
Figure 15. An analysis of the spatially resolved spectra of the galaxy observed with H#009. The left-most panel shows the field of the hexabundle (red circle, diameter 15 arcsec) superimposed on a United Kingdom Schmidt Telescope (UKST) b_J-band image from SuperCOSMOS (Hambly et al. 2001); the image is 1×1 arcmin in size. The other two panels show the spatially resolved line ratio maps for the galaxy, with [N II]λ6583/Hα in the centre and [O III]λ5007/Hβ to the right.

Gas kinematics were examined for six of the galaxies using the Hα emission line. In each spaxel of each galaxy the Hα line was fitted by a Gaussian function and the kinematic properties (mean velocity and velocity dispersion) extracted from the fit. The resulting velocity maps are shown in Fig. 16. The colour bars show velocity in km s^{-1}. From these maps it is clear the galaxies H#009, H#010,

H#012 and H#016 are fairly typical rotating discs; the velocity maps for H#001 and H#004 are possibly more complex.

From the wealth of spatially resolved information presented for the handful of galaxies studied in this single field during the commissioning run, it is clear that SAMI can explore a very wide parameter space with enormous science potential.
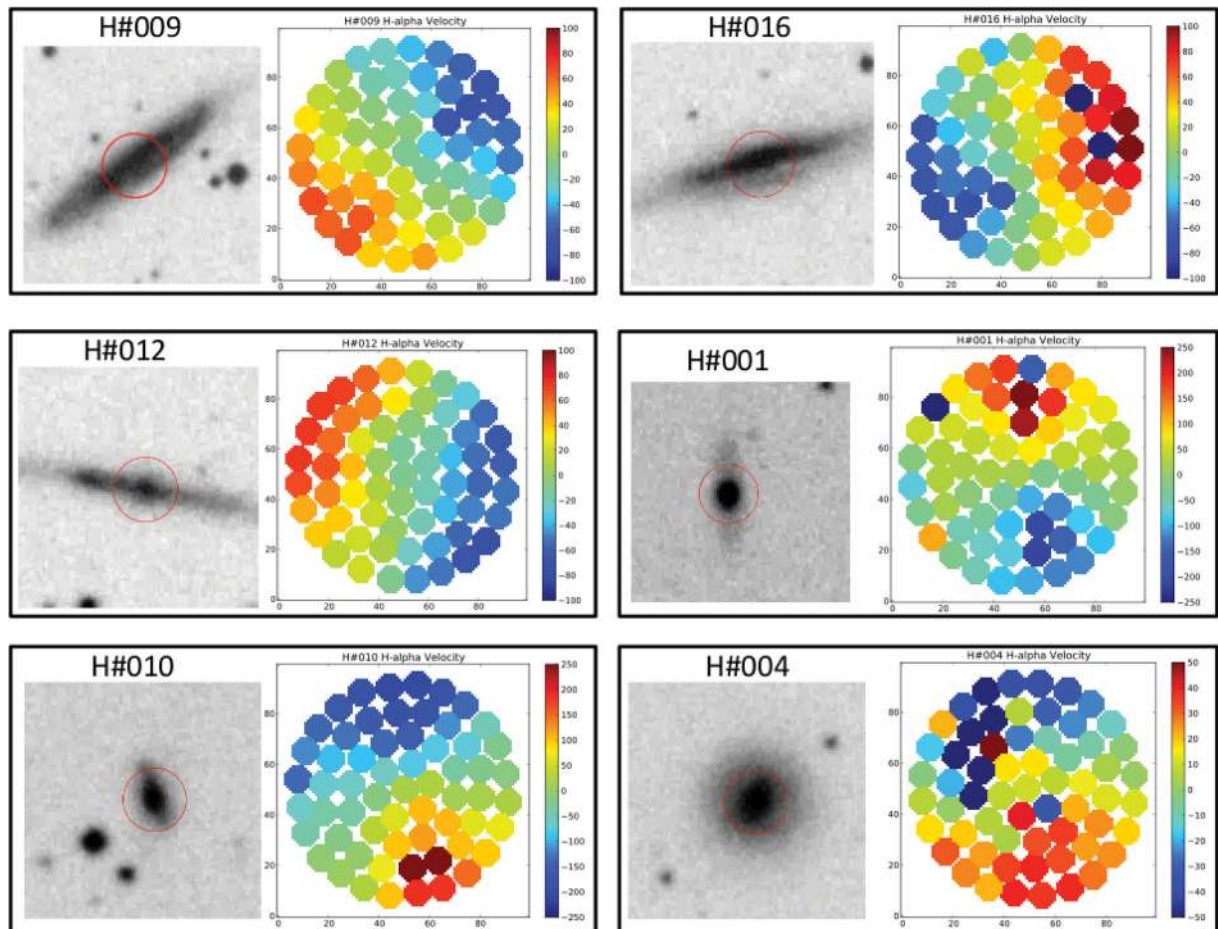

Figure 16. Gas kinematics for six of the SAMI galaxies. On the left is a SuperCOSMOS (Hambly et al. 2001) b_J-band image of each galaxy, with the IFU FoV represented by the red circle. Each image is $\sim$1 arcmin on a side. The SAMI Hα velocity maps are shown on the right-hand side, with the X and Y coordinates in pixel units and the velocity scale in km s^{-1}.

6 CONCLUSIONS

In this paper we have presented a new instrument, SAMI which, makes use of astrophotonic technology in the form of hexabundles (multi-core fibre bundles) to enable simultaneous IFU observations of 13 objects over a 1-degree diameter accessible field. Each IFU contains 61 elements, each 1.6 arcsec in diameter, giving an FoV for each IFU of 15 arcsec. SAMI has now been commissioned on the AAT and we demonstrate its science potential via preliminary observations of galaxies selected from the 6dF Galaxy Survey.

We make the case that multiplexed integral field spectroscopy is the natural next step in galaxy surveys, which to date have been dominated by multiplexed single-aperture observations. The extra information gained by IFU spectroscopy, combined with the statistical power of a large survey, will enable a fundamental step forward in our understanding of galaxy formation and evolution by distinguishing the spectroscopic properties of the major structural components of galaxies. Assuming that a survey could observe three fields per night (i.e. nominal exposure times between 2 and 3 h), SAMI will allow 10 000 galaxies to be targeted in 260 clear nights on the AAT.

Much greater gains could be made with an increased FoV and larger numbers of IFUs. A key requirement for making full use of the larger fields of view available on current and future telescopes is to have sufficient spectrographs to handle all the fibres from the IFUs. A 2-degree diameter FoV (e.g. that available with the AAT's 2dF corrector) could accommodate ∼50 or more IFU bundles comparable to those in SAMI; this would, however, require ∼3300 fibres (including sky fibres). Such large numbers of fibres naturally drive designs towards mass-produced fixed-format spectrographs, such as those currently being developed for projects such as the Multi Unit Spectroscopic Explorer (MUSE) (Bacon et al. 2004) and VIRUS (Hill et al. 2006).

More developmental work on the bundle technology is under way. One possible improvement is to force the fibre cores into a perfect hexagonal configuration to simplify the data analysis, particularly when using dithering to smooth out the discrete sampling. This will not be easy to do with our current core size while at the same time ensuring an AR-coated polished front facet that is not overly stressed by the hexagonal grid. With the successful commissioning on the AAT of fibre-based OH suppression technology (Bland-Hawthorn, Englund & Edvell 2004; Ellis et al. 2010), we can envisage whole bundles that are fully sky-suppressed at near-infrared wavelengths. Once the near-infrared sky is rendered as dark as the optical sky, exposure times in both regimes are expected to be the same and it makes sense to run optical and infrared spectrographs simultaneously.

ACKNOWLEDGMENTS

REFERENCES

Abazajian K. et al., 2003, AJ, 126, 2081
Bacon R. et al., 2001, MNRAS, 326, 23
Bacon R. et al., 2004, in Moorwood A. F. M., Iye M., eds, SPIE Conf. Ser. Vol. 5492, Ground based instrumentation for Astronomy. Glasgow, p. 1145
Baldry I. K., Glazebrook K., Brinkmann J., Ivezić Ž., Lupton R. H., Nichol R. C., Szalay A. S., 2004, ApJ, 600, 681
Baldry I. K., Glazebrook K., Driver S. P., 2008, MNRAS, 388, 945
Baldwin J. A., Phillips M. M., Terlevich R., 1981, PASP, 93, 5
Balogh M. L., McGee S. L., 2010, MNRAS, 402, L59
Bardeen J. M., Bond J. R., Kaiser N., Szalay A. S., 1986, ApJ, 304, 15
Barden S. C., Ramsey L. W., Truax R. J., 1981, PASP, 93, 154
Bekki K., 2009, MNRAS, 399, 2221
Berta Z. K., Jimenez R., Heavens A. F., Panter B., 2008, MNRAS, 391, 197
Binney J., 1992, ARA&A, 30, 51
Binney J., Nipoti C., Fraternali F., 2009, MNRAS, 397, 1804
Bland-Hawthorn J., 2009, in Andersen J., Bland-Hawthorn J., Nordström B., eds, IAU Symp. Vol. 254, The Galaxy disk in Cosmological Context. Cambridge Univ. Press, p. 241
Bland-Hawthorn J., Kern P., 2009, Opt. Express, 17, 1880
Bland-Hawthorn J., Englund M., Edvell G., 2004, Opt. Express, 12, 5902
Bland-Hawthorn J., Sutherland R., Agertz O., Moore B., 2007, ApJ, 670, L109
Bland-Hawthorn J. et al., 2011, Opt. Express, 19, 2649
Blanton M. R., Eisenstein D., Hogg D. W., Schlegel D. J., Brinkmann J., 2005, ApJ, 629, 143
Bournaud F., Dekel A., Teyssier R., Cacciato M., Daddi E., Juneau S., Shankar F., 2011, ApJL, 741, 33
Bower R. G., Benson A. J., Malbon R., Helly J. C., Frenk C. S., Baugh C. M., Cole S., Lacey C. G., 2006, MNRAS, 370, 645
Briggs F. H., 1990, ApJ, 352, 15
Brough S., Proctor R., Forbes D. A., Couch W. J., Collins C. A., Burke D. J., Mann R. G., 2007, MNRAS, 378, 1507
Brough S., Tran K.-V., Sharp R. G., von der Linden A., Couch W. J., 2011, MNRAS, 414, L80
Brunino R., Trujillo I., Pearce F. R., Thomas P. A., 2007, MNRAS, 375, 184
Bryant J. J., O'Byrne J. W., Bland-Hawthorn J., Leon-Saval S. G., 2011, MNRAS, 415, 2173
Campbell L., 2009, PhD thesis, Australian National University
Cappellari M., 2008, MNRAS, 390, 71
Cappellari M. et al., 2011a, MNRAS, 413, 813
Cappellari M. et al., 2011b, MNRAS, 416, 1680
Cattaneo A., Dekel A., Devriendt J., Guiderdoni B., Blaizot J., 2006, MNRAS, 370, 1651
Chiappini C., Matteucci F., Gratton R., 1997, ApJ, 477, 765
Christlein D., Zaritsky D., Bland-Hawthorn J., 2010, MNRAS, 405, 2549
Colless M. et al., 2001, MNRAS, 328, 1039
Conti A. et al., 2003, AJ, 126, 2330
Cowie L. L., Songaila A., Hu E. M., Cohen J. G., 1996, AJ, 112, 839
Cox D. P., 2005, ARA&A, 43, 337
Croom S. M., Smith R. J., Boyle B. J., Shanks T., Miller L., Outram P. J., Loaring N. S., 2004a, MNRAS, 349, 1397
Croom S., Saunders W., Heald R., 2004b, Anglo-Australian Observatory Epping Newsletter, 106, 12
Croom S. M. et al., 2005, MNRAS, 356, 415
Croom S. M. et al., 2009, MNRAS, 399, 1755
Croton D. J. et al., 2006, MNRAS, 365, 11
Davis M. et al., 2007, ApJ, 660, L1
De Propris R., Conselice C. J., Liske J., Driver S. P., Patton D. R., Graham A. W., Allen P. D., 2007, ApJ, 666, 212

Dekel A. et al., 2009, Nat, 457, 451

Dettmar R. J., 1992, Fundamentals Cosmic Phys., 15, 143

Dressler A., 1980, ApJ, 236, 351

Dressler A. et al., 1997, ApJ, 490, 577

Driver S. P., Allen P. D., Liske J., Graham A. W., 2007, ApJ, 657, L85

Driver S. P. et al., 2011, MNRAS, 413, 971

Dutton A. A., Conroy C., van den Bosch F. C., Prada F., More S., 2010, MNRAS, 407, 2

Ellis S. C., Driver S. P., Allen P. D., Liske J., Bland-Hawthorn J., De Propris R., 2005, MNRAS, 363, 1257

Ellis S. C. et al., 2010, in Mclean I. S., Ramsay S. K., Takami H., eds, SPIE Conf. Ser. Vol. 7735, Ground based and Airbourne Instrumentation for Astronomy III. SPIE, Bellingham

Ellison S. L., Patton D. R., Simard L., McConnachie A. W., 2008, AJ, 135, 1877

Emsellem E. et al., 2007, MNRAS, 379, 401

Emsellem E. et al., 2011, MNRAS, 414, 888

Fakhouri O., Ma C.-P., 2008, MNRAS, 386, 577

Ferrarese L., Merritt D., 2000, ApJ, 539, L9

Gaensler B. M., Madsen G. J., Chatterjee S., Mao S. A., 2008, PASA, 25, 184

Gebhardt K. et al., 2000, ApJ, 539, L13

Genzel R. et al., 2008, ApJ, 687, 59

Gómez P. L. et al., 2003, ApJ, 584, 210

Goodwin M., Smedley S., Barnes S., Farrell T., Barden S., 2010, in Mclean I. S., Ramsay S. K., Takami H., eds, SPIE Conf. Ser. Vol. 7735, Ground based and Airbourne Instrumentation for Astronomy III. SPIE, Bellingham

Gray P. M., 1983, in Baker L. R., ed., SPIE Conf. Ser. Vol. 374, Fibre Optics '83, p. 160

Gunn J. E., Gott J. R., III, 1972, ApJ, 176, 1

Hambly N. C. et al., 2001, MNRAS, 326, 1279

Hasinger G., Miyaji T., Schmidt M., 2005, A&A, 441, 417

Heckman T. M., 1980, A&A, 87, 152

Heckman T. M., Kauffmann G., Brinchmann J., Charlot S., Tremonti C., White S. D. M., 2004, ApJ, 613, 109

Hill G. J., MacQueen P. J., Tejada C., Cobos F. J., Palunas P., Gebhardt K., Drory N., 2004, in Moorwood A. F. M., Iye M., eds, SPIE Conf. Ser. Vol. 5492, Ground based and Airbourne Instrumentation for Astronomy. SPIE, Bellingham, p. 251

Hill G. J., MacQueen P. J., Palunas P., Kelz A., Roth M. M., Gebhardt K., Grupp F., 2006, New Astron. Rev., 50, 378

Ho L. C., 2008, ARA&A, 46, 475

Hog E., Kuzmin A., Bastian U., Fabricius C., Kuimov K., Lindegren L., Makarov V. V., Roeser S., 1998, A&A, 335, L65

Hopkins A. M., Beacom J. F., 2006, ApJ, 651, 142

Hopkins P. F., Hernquist L., 2009, ApJ, 694, 599

Hopkins P. F., Hernquist L., Cox T. J., Kereš D., 2008, ApJS, 175, 356

Jarrett T. H., Chester T., Cutri R., Schneider S., Skrutskie M., Huchra J. P., 2000, AJ, 119, 2498

Jones D. H. et al., 2004, MNRAS, 355, 747

Jones D. H., Saunders W., Read M., Colless M., 2005, PASA, 22, 277

Jones D. H. et al., 2009, MNRAS, 399, 683

Jones B. J. T., van de Weygaert R., Aragón-Calvo M. A., 2010, MNRAS, 408, 897

Kaiser N., 1984, ApJ, 284, L9

Kapferer W., Sluka C., Schindler S., Ferrari C., Ziegler B., 2009, A&A, 499, 87

Kauffmann G. et al., 2003, MNRAS, 346, 1055

Kelz A., Roth M. M., 2006, New Astron. Rev., 50, 355

Kewley L. J., Ellison S. L., 2008, ApJ, 681, 1183

Kewley L. J., Dopita M. A., Sutherland R. S., Heisler C. A., Trevena J., 2001, ApJ, 556, 121

Kewley L. J., Groves B., Kauffmann G., Heckman T., 2006, MNRAS, 372, 961

Kimura M. et al., 2010, PASJ, 62, 1135

King A. R., Pounds K. A., 2003, MNRAS, 345, 657

Kissler-Patig M., Copin Y., Ferruit P., Pécontal-Rousset A., Roth M. M., 2004, Astron. Nachr., 325, 159

Kobayashi C., 2004, MNRAS, 347, 740

Kormendy J., Kennicutt R. C., Jr, 2004, ARA&A, 42, 603

Krajnović D., Cappellari M., de Zeeuw P. T., Copin Y., 2006, MNRAS, 366, 787

Larson R. B., Tinsley B. M., Caldwell C. N., 1980, ApJ, 237, 692

Le Fèvre O. et al., 2005, A&A, 439, 845

Lee J., 2004, ApJ, 614, L1

Lee J., Erdogdu P., 2007, ApJ, 671, 1248

Lee J., Pen U.-L., 2000, ApJ, 532, L5

Lewis I. et al., 2002, MNRAS, 334, 673

Li C., Kauffmann G., Heckman T. M., Jing Y. P., White S. D. M., 2008a, MNRAS, 385, 1903

Li C., Kauffmann G., Heckman T. M., White S. D. M., Jing Y. P., 2008b, MNRAS, 385, 1915

López-Sánchez Á. R., 2010, A&A, 521, A63

López-Sánchez Á. R., Esteban C., 2008, A&A, 491, 131

López-Sánchez A. R., Esteban C., 2009, A&A, 508, 615

Lopez-Sanchez A. R., Koribalski B., van Eymeren J., Esteban C., Kirby E., Jerjen H., Lonsdale N., 2012, MNRAS, 419, 1051

McCarthy I. G., Frenk C. S., Font A. S., Lacey C. G., Bower R. G., Mitchell N. L., Balogh M. L., Theuns T., 2008, MNRAS, 383, 593

Madsen G. J., Haffner L. M., Reynolds R. J., 2006, Memoire della Societa Astronomica Italiana, 77, 1163

Marinacci F., Fraternali F., Nipoti C., Binney J., Ciotti L., Londrillo P., 2011, MNRAS, 415, 1534

Martin C. L., 1998, ApJ, 506, 222

Masters K. L. et al., 2010, MNRAS, 405, 783

Nichols M., Bland-Hawthorn J., 2011, ApJ, 732, 17

Nikolic B., Cullen H., Alexander P., 2004, MNRAS, 355, 874

Oliveira A. C., de Oliveira L. S., dos Santos J. B., 2005, MNRAS, 356, 1079

Pasquini L. et al., 2002, The Messenger, 110, 1

Patton D. R., Atfield J. E., 2008, ApJ, 685, 235

Paz D. J., Stasyszyn F., Padilla N. D., 2008, MNRAS, 389, 1127

Peebles P. J. E., 1969, ApJ, 155, 393

Pen U.-L., Lee J., Seljak U., 2000, ApJ, 543, L107

Pracy M. B., Kuntschner H., Couch W. J., Blake C., Bekki K., Briggs F., 2009, MNRAS, 396, 1349

Press W. H., Flannery B. P., Teukolsky S. A., 1986, Numerical Recipes. The Art of Scientific Computing. Cambridge Univ. Press, Cambridge

Quillen A. C., Frogel J. A., Gonzalez R. A., 1994, ApJ, 437, 162

Rand R. J., 1996, ApJ, 462, 712

Randall S., Nulsen P., Forman W. R., Jones C., Machacek M., Murray S. S., Maughan B., 2008, ApJ, 688, 208

Reyes R., Mandelbaum R., Gunn J. E., Nakajima R., Seljak U., Hirata C. M., 2011, preprint (arXiv e-prints)

Richards G. T. et al., 2006, AJ, 131, 2766

Sánchez S. F. et al., 2011, A&A, submitted

Sancisi R., Fraternali F., Oosterloo T., van der Hulst T., 2008, A&AR, 15, 189

Sanders D. B., Soifer B. T., Elias J. H., Madore B. F., Matthews K., Neugebauer G., Scoville N. Z., 1988, ApJ, 325, 74

Schawinski K. et al., 2009, MNRAS, 396, 818

Scoville N. et al., 2007, ApJS, 172, 1

Shapiro K. L. et al., 2008, ApJ, 682, 231

Sharma S., Steinmetz M., 2005, ApJ, 628, 21

Sharp R., Birchall M. N., 2010, PASA, 27, 91

Sharp R. G., Bland-Hawthorn J., 2010, ApJ, 711, 818

Sharp R., Parkinson H., 2010, MNRAS, 408, 2495

Sharp R. et al., 2006, in McLean I. S., Iye M., eds, SPIE Conf. Ser. Vol. 6269, Ground based and Airbourne Instrumentation for Astronomy. SPIE, Bellingham

Shaver P. A., McGee R. X., Newton L. M., Danks A. C., Pottasch S. R., 1983, MNRAS, 204, 53

Simard L., Mendel J. T., Patton D. R., Ellison S. L., McConnachie A. W., 2011, ApJS, 196, 11

Smith G. A. et al., 2004, in Moorwood A. F. M., Iye M., eds, SPIE Conf Ser. Vol. 5492, Ground based and Airbourne Instrumentation for Astronomy. SPIE, Bellingham, p. 410

Smith M. C. et al., 2007, MNRAS, 379, 755

Spolaor M., Proctor R. N., Forbes D. A., Couch W. J., 2009, ApJ, 691, L138

Springob C. M., Masters K. L., Haynes M. P., Giovanelli R., Marinoni C., 2007, ApJS, 172, 599

Springob C. M. et al., 2011, preprint (arXiv e-prints)

Staveley-Smith L., Bland J., Axon D. J., Davies R. D., Sharples R. M., 1990, ApJ, 364, 23

Steinmetz M., Mueller E., 1994, A&A, 281, L97

Strateva I. et al., 2001, AJ, 122, 1861

Strickland D. K., 2007, MNRAS, 376, 523

Su D. Q., Cui X., Wang Y., Yao Z., 1998, in Stepp L. M., ed., SPIE Conf. Ser. Vol. 3352, Advanced Technology Optical/IR Telescopes VI, p. 76

Sun M., Donahue M., Voit G. M., 2007, ApJ, 671, 190

Taylor E. N., Franx M., Brinchmann J., van der Wel A., van Dokkum P. G., 2010, ApJ, 722, 1

Thomas D., Maraston C., Bender R., Mendes de Oliveira C., 2005, ApJ, 621, 673

Tremaine S. et al., 2002, ApJ, 574, 740

Trujillo I., Carretero C., Patiri S. G., 2006, ApJ, 640, L111

Tully R. B., Fisher J. R., 1977, A&A, 54, 661

Vila Costas M. B., Edmunds M. G., 1992, MNRAS, 259, 121

Wallace P. T., 1994, in Crabtree D. R., Hanisch R. J., Barnes J., eds, ASP Conf. Ser. Vol. 61, Astronomical Data Analysis Software and Systems III, Astron. Soc. Pac., San Francisco, p. 481

Welikala N., Connolly A. J., Hopkins A. M., Scranton R., Conti A., 2008, ApJ, 677, 970

Welikala N., Connolly A. J., Hopkins A. M., Scranton R., 2009, ApJ, 701, 994

White S. D. M., Rees M. J., 1978, MNRAS, 183, 341

Wisnioski E. et al., 2011, MNRAS, 417, 2601

Yan R., Blanton M. R., 2011, preprint (arXiv e-prints)

Yang Y. et al., 2008, A&A, 477, 789

York D. G. et al., 2000, AJ, 120, 1579

Zaritsky D., Rix H.-W., 1997, ApJ, 477, 118

Zhang Y., Yang X., Faltenbacher A., Springel V., Lin W., Wang H., 2009, ApJ, 706, 747

This paper has been typeset from a TeX/LaTeX file prepared by the author.